HESSIAN-INVERSION-FREE RAY-BORN INVERSION FOR QUANTITATIVE ULTRASOUND TOMOGRAPHY

ASHKAN JAVAHERIAN

Department of Medical Physics & Biomedical Engineering,
University College London, London, UK. WC1E 6BT

Abstract

This study proposes a Hessian-inversion-free ray-born inversion approach for biomedical ultrasound tomography. The proposed approach is a more efficient version of the ray-born inversion approach proposed in [3]. Using these approaches, the propagation of acoustic waves are modelled using a ray approximation to heterogeneous Green's function, and the inverse problem is solved in the frequency domain via iteratively linearisation and minimisation of the objective function from low to high frequencies. In [3], the linear subproblem associated with each frequency interval is solved via an implicit and iterative inversion of the Hessian matrix (inner iterations). Instead, in this study, each linear subproblem is weighted in a way in which the Hessian matrix be diagonalised, and can thus be inverted in a single step. Using the proposed approach, the computational cost of solving each associated linear subproblem becomes almost the same as solving one linear subproblem associated with a radon-type time-of-flight-based approach using bent rays. More importantly, the assumptions made for diagonalising the Hessian matrix make the image reconstruction more stable than the inversion approach in [3] to noise.

1. Introduction

The aim of ultrasound tomography (UST) is to determine the map of the acoustic properties of the interior of an object from ultrasonic measurements made on its boundary. Ultrasound tomography has received growing interest for biomedical diagnostic applications [4, 5, 6]. One of the most important application of UST for medical diagnosis is detection of malignant tumours in the breast [4, 7, 8, 9, 10]. Ideally, the information which can be determined from ultrasound data measured on the boundary of an object include the quantitative distribution of the sound speed, absorption and density, and a qualitative map of reflectivity [6]. This manuscript is concentrated on reconstruction of the sound speed, so the term UST is used for the sound speed reconstruction. Approaches to image reconstruction of the sound speed from UST data can be categorised by: 1) the data type used in the inversion, 2) whether the objective function to be minimised is nonlinear or linearised, 3) whether the objective function is defined in the time domain or frequency domain, or 4) the forward model used.

In terms of the data type used, the first class of approaches use only the direct times-of-flight between the emitters and receivers [11], and no scattered waves are included. The second uses the complete measured time series, including the scattered waves [12, 13, 14, 15, 16, 17, 18, 19, 20, 21].

E-mail address: a.javaherian@ucl.ac.uk.
Date: June 2023.

The third uses the direct-arrival and first-scattered waves [22, 23, 24, 25, 40, 27, 28, 29, 30, 31]. In our study, the first and third data types are used, the former for providing an initial guess and the latter for solving the main inverse problem. The chosen approach for solving the main inverse problem is based on an iterative linearisation of the objective function, and performs the linearisations in the frequency domain from low to high frequencies. The forward problem is modelled based on a ray-approximation to the heterogeneous Green's function. The motivation for choosing this forward model is that ray theory based on the high frequency approximation provides a good trade-off between accuracy and computational cost when data is broadband [32]. In addition, the known limitations of ray theory such as caustics or mutivaluedness of the minimal acoustic length [33] are less challenging for imaging soft tissues like the breast with refractive index often varying between $0.9 - 1.1$ than seismic imaging applications with sharp changes in the refractive index. The details of the proposed UST inversion approach were given in [3]. It was numerically shown that this approach can reconstruct a high resolution map of the sound speed, but it is computationally a few orders of magnitude less costly than full-waveform inversion approaches which use the full solution of the wave equation [12, 15, 16].

The common approaches accounting for diffraction or singly scattered waves use the Green's function in the homogeneous medium, and account for the acoustic heterogeneity only in the scattering potential [22, 23, 24, 25, 40, 27, 28, 31], but it was shown that combining ray theory with Born inversion can significantly improve the accuracy via including the sound speed heterogeneity, refraction and acoustic absorption and dispersion in the Green's functions predicting the incident and scattered waves [3]. In [34], a single-stage inversion approach which combines the diffraction tomography with ray tracing was proposed. Using this approach, the phase aberration of the Green's function because of heterogeneities was accounted for by performing ray tracing on an image reconstructed using a time-of-flight-based approach.

The UST inversion approach proposed in [3] fits into a class of linearised inversion approaches, known as ray-born migration/inversion, in the context of inverse seismic theory [32, 35, 36, 37]. In [3], the objective function is discretised in the frequency domain, and is linearised and minimised over the frequency range covered by the ultrasound transducers. This is done by dividing the frequency range into a number of frequency intervals, each including a fixed number, here 2, of the discretised frequencies, and performing the minimisation sequentially from low to high frequency intervals such that the solution of the linearised subproblem for each frequency interval is used as initial guess for the linearised subproblem associated with the next frequency interval. Because the inverse problem of reconstructing acoustic parameters from ultrasound or seismic data is nonlinear, minimising the objective function from low to high frequencies helps avoiding getting stuck in the local minima [13, 14, 31].

In [3], each linearised subproblem, which is equivalent to the product of an inverse of the Hessian matrix by the gradient of the objective function, is solved implicitly using a Conjugate Gradient (CG) algorithm via an iterative implementation of the Fréchet derivative of the forward operator and its adjoint. Because of the iterative computation of the Hessian matrix, the computational cost for solving each linearised subproblem using this approach becomes about an order of magnitude more than solving a linearised subproblem associated with a Radon-type time-of-flight-based approach, whose major computational cost corresponds to only two-point ray tracing. (Nevertheless, using the CPU mentioned in section 6.3, the total computational time for image reconstruction using the inversion approach in [3] is almost the same as numerically solving a single forward problem of the full-Waveform inversion using a k-space pseudo-spectral approach for simulating propagation of acoustic waves [39, 40, 41, 42, 43].) For further reducing the computational cost, this study proposes a single-stage approach for solving the linearised subproblem associated with

each frequency set. The proposed approach is based on weighting the arising linearised subproblems such that the Hessian matrix becomes diagonalised and can thus be inverted in a single step. Using the proposed approach, the computational cost of each iteration (linearised subproblem) of the ray-Born minimisation approach is reduced to almost that of a Radon-type time-of-flight-based inversion approach using bent rays [38].

Section 2 introduces the forward and inverse problems of UST based on a Green's function solution to the frequency-domain Helmholtz wave equation for heterogeneous and absorbing media. In section 3, the proposed approach for solving the inverse problem based on the heterogeneous Green's function is explained. Section 4 describes ray tracing and how the Green's function for heterogeneous media is approximated based on ray theory. Section 5 explains the procedure for discretising the forward and inverse problems. In section 6, the ray approximation to the heterogeneous Green's function is numerically validated, and the reconstructed images demonstrating the performance of the proposed Hessian-inversion-free ray-born inversion approach are presented, and compared to the inversion approach in [3].

Simulation of wave propagation as benchmark. In the appendix-A, the numerical approach used in this study for an accurate simulation of acoustic waves produced by an omnidirectional point and time varying source using a k-space pesudospectral method is briefly discussed. (The readers are referred to [43] for further details.) This numerical approach has been widely used for numerically solving the wave equation [39, 40, 41]. A numerical implementation of this approach is also available as an open-source toolbox [42]. The k-Wave Version 1.3, the most recent version at the time of submitting the first version of this manuscript, was used in this study, but the inclusion of time-varying source in this toolbox was found to be inconsistent with the wave equation, and was thus corrected to match with the wave equation and its analytic solution [43]. (No changes have been reported in the most recent version 1.4 regarding the inclusion of time-varying source, but the readers can check.)

2. Green's function solution to the wave equation

This section describes the forward and inverse problems of image reconstruction of the sound speed. Let $\boldsymbol{x} = \left(x^1, ..., x^d\right)$ denote a spatial position in $\mathbb{R}^d$ with d the number of dimensions. In general, d can be either 2 or 3. This study is restricted to $d = 2$, but it can be extended to $d = 3$. Accordingly, $\Omega \subset \mathbb{R}^d$ is an open bounded set, and contains the spatially-varying part of the sound speed distribution, $c(\boldsymbol{x})$, i.e., $(c(\boldsymbol{x})/c_0 - 1) \in c_0^\infty$, where c_0 is a scalar value representing the sound speed outside Ω (here the sound speed in water). The open set Ω is bounded by a circular ring $\mathbb{S} \subset \mathbb{R}^{d-1}$, which contains the emission and reception elements e and r. (The emission and reception elements are assumed points.) Each emission element, referred to here as emitter $e \in \{1, ..., N_e\}$ and centred at $\boldsymbol{x}_e$, is sequentially excited by a pulse and acts as a source $s(t; \boldsymbol{x}_e)$ within the excitation time $t \in (0, T_s)$. The acoustic pressure field produced by each emitter propagates across the object in water and is measured at the reception elements, referred to here as receiver $r \in \{1, ..., N_r\}$ and centred at $\boldsymbol{x}_r$, for times $t \in (0, T)$ with $T \gg T_s$. For each excitation element e, the time series measured by the receiver r is represented by $p(t, \boldsymbol{x}_r; \boldsymbol{x}_e)$. The inverse problem is an image reconstruction of $c(x)$ from the measured boundary pressure times series $p(t, \boldsymbol{x}_r; \boldsymbol{x}_e)$ for all emitter-receiver pairs.

While the data is typically measured in the time domain, i.e. with a broadband excitation signal, the image reconstruction is here performed in the frequency domain. To this end, we define the

following Fourier transform pair between the time and temporal frequency domains,

$$\hat{p}(\omega) = \mathscr{F} p(t) = \int_{-\infty}^{\infty} p(t) e^{i\omega t} dt, \quad p(t) = \mathscr{F}^{-1} \hat{p}(\omega) = \frac{1}{2\pi} \int_{-\infty}^{\infty} \hat{p}(\omega) e^{-i\omega t} dt. \tag{1}$$

2.1. **Lossy Helmholtz equation and complex wavevector.** The propagation of a single frequency acoustic pressure field, $\hat{p}(\omega, \boldsymbol{x})$, in an absorbing medium is often modelled using a lossy Helmholtz equation of the form

$$\left(\tilde{k}(\boldsymbol{x})^2 + \nabla^2\right) \hat{p}(\omega, \boldsymbol{x}; \boldsymbol{x}_e) = -s(\omega, \boldsymbol{x}_e), \quad \tilde{k}^2 = |\tilde{\boldsymbol{k}}|^2, \tag{2}$$

where $\tilde{\boldsymbol{k}}$ is a complex wavevector $\tilde{\boldsymbol{k}} = \boldsymbol{k} + i\boldsymbol{k}_i$, where the real part $\boldsymbol{k}$ is related to the phase speed $c_p(\omega)$ of the wave by

$$|\boldsymbol{k}| \equiv k = \omega / c_p(\omega), \tag{3}$$

and the imaginary part is related to the absorption coefficient α by

$$\boldsymbol{k}_i = \alpha \, \boldsymbol{k}/k. \tag{4}$$

The specific from of the wavenumber we use is based on Szabo's absorption model, and is in the form [44]

$$\begin{aligned} \tilde{k} &= \frac{\omega}{c} - \frac{\alpha_0 (-i)^{y+1} \omega^y}{\cos(\pi y/2)} \\ &= \frac{\omega}{c} + \alpha \, \left(\tan(\pi y/2) + i \right) = k + i\alpha, \end{aligned} \tag{5}$$

where the scalar α is acoustic absorption and follows the frequency power law, $\alpha = \alpha_0 \omega^y$. Here, α_0 has units $\mathrm{Np}(\mathrm{rad/s})^{-y}\mathrm{m}^{-1}$, and y is the power-law exponent with a non-integer often in the range $1 < y \leqslant 1.5$ for soft tissue [45, 46]. In (5), $(-i)^y = \cos(\pi y/2) - i \, \sin(\pi y/2)$ has been used. Using the specific form (5), the phase speed satisfies

$$\frac{1}{c_p(\omega)} = \frac{k}{\omega} = \frac{1}{c} + \alpha_0 \, \tan(\pi y/2) \, \omega^{(y-1)}. \tag{6}$$

For further details, see [44]. The solution of (2) in terms of Green's function can be written as

$$\hat{p}(\omega, \boldsymbol{x}) = \int g(\omega, \boldsymbol{x}; \boldsymbol{x}') s(\omega, \boldsymbol{x}') d\boldsymbol{x}', \tag{7}$$

where $g(\omega, \boldsymbol{x}; \boldsymbol{x}')$ is the Green's function associated with frequency ω, at point $\boldsymbol{x}$ and originated at point $\boldsymbol{x}'$, and satisfies

$$\left(\tilde{k}(\boldsymbol{x})^2 + \nabla^2\right) g(\omega, \boldsymbol{x}; \boldsymbol{x}') = -\delta(\boldsymbol{x} - \boldsymbol{x}'). \tag{8}$$

For the 2D case and in heterogeneous and absorbing media, the Green's function associated with frequency ω, at point $\boldsymbol{x}$ and originated at $\boldsymbol{x}'$, can be written in the form

$$g(\omega, \boldsymbol{x}; \boldsymbol{x}') \approx A(\omega, \boldsymbol{x}; \boldsymbol{x}') \exp\left(i(\phi(\omega, \boldsymbol{x}; \boldsymbol{x}') + \pi/4)\right). \tag{9}$$

Here, ϕ is the phase, and $A = A_{abs} A_{geom}$ is the amplitude factor, and contains contributions from absorption as well as geometric spreading. All these parameters are approximated using the ray theory [33].

3. Minimisation approach

This section explains the approach taken for minimising the objective function. Following [3], the objective function is linearised at a number of discretised frequencies within the frequency range of the ultrasound transducers, and the arising linearised subproblems are solved from low to high frequencies. The naive form of each linearised subproblem is equivalent to computing the product of an implicit inverse of the Hessian matrix by the gradient of the objective function, and can be performed iteratively via computing the product of the Hessian matrix by perturbations to the unknown parameter of interest until the perturbation which minimises the associated linearised objective function is determined [3]. Instead, here, each linearised subbproblem is weighted in both data and solution spaces so that the Hessian matrix be diagonalised and can thus be inverted in a single step. In [3], the objective function was minimised in terms of the sound speed c, but here, the objective function is minimised in terms of the squared slowness, $m = 1/c^2$, in order to simplify diagonalisation of the Hessian matrix. Accordingly, the objective function in terms of the Green's function in the frequency domain is defined in the form

$$\mathcal{F}(m) = \frac{1}{2} \sum_{e,r} \int \delta g_{res}(m;\omega,r;e)^* \; \mathcal{Q}_g(m;\omega,r,e) \; \delta g_{res}(m;\omega,r;e) \; d\omega, \tag{10}$$

where $*$ denotes the complex conjugate, and $\mathcal{Q}_g(m;\omega,r,e)$ is a component of a diagonal matrix which weights the objective function in data space (ω,r,e), and will be derived later. Also, δg_{res} is the *residual*, and is in the form

$$\delta g_{res}(m;\omega,r;e) = g(m;\omega,r;e) - \hat{g}_{(\omega,r;e)}. \tag{11}$$

Here, $g_{(m;\omega,r;e)}$ and $\hat{g}_{(\omega,r;e)}$ are termed the *approximated* and *measured* Green's functions associated with frequency ω, at point $\boldsymbol{x}_r$ and originated at point $\boldsymbol{x}_e$. Note that $\hat{g}_{(\omega,r;e)}$ can be obtained by deconvolution of the measured pressure $\hat{p}_{(\omega,r;e)}$ from the pressure source $s(\omega,\boldsymbol{x}_e)$ in the frequency domain. (Equivalent formulae can be obtained using the objective function in terms of the pressure data [3].)

The nth linearisation of the objective function (10) around the squared slowness $m^{(n)}$ yields

$$\delta m^{(n)} \approx \underset{\delta m}{\arg\min} \; \frac{1}{2} \sum_{e,r} \int \big(\delta g^{(n)}_{(\omega,r,e)}(\delta m) + \delta g^{(n)}_{res}(\omega,r,e)\big)^* \; \mathcal{Q}^{(n)}_g(\omega,r,e) \big(\delta g^{(n)}_{(\omega,r,e)}(\delta m) + \delta g^{(n)}_{res}(\omega,r,e)\big) \; d\omega, \tag{12}$$

where $\mathcal{Q}^{(n)}_g(\omega,r,e) := \mathcal{Q}_g(m^{(n)};\omega,r,e)$ and $\delta g^{(n)}_{res}(\omega,r,e) := \delta g_{res}(m^{(n)};\omega,r;e)$ have been used for brevity, and will be applied from now on. The problem (12) seeks to find the perturbation $\delta m^{(n)}$, which fits the vector of the induced perturbation to Green's function on receivers to the minus residual in data space (ω,r,e). The perturbed Green's function $\delta g^{(n)}_{(\omega,r,e)}(\delta m)$ is in the form

$$\delta g^{(n)}_{(\omega,r,e)}(\delta m) = \int \frac{\partial g^{(n)}(\omega,r;e)}{\partial m^{(n)}(\boldsymbol{x}')} \delta m(\boldsymbol{x}') \; d\boldsymbol{x}'. \tag{13}$$

Here, $g^{(n)}(\omega,r;e) := g(m^{(n)},\omega,r;e)$, and $\partial g^{(n)}(\omega,r;e)/\partial m^{(n)}(\boldsymbol{x}')$ is a component of the Fréchet derivative of the Green's function on receivers with respect to the squared slowness m. The Fréchet derivative operator linearly acts on the perturbation δm, and its components are in the form

$$\frac{\partial g^{(n)}(\omega,r;e)}{\partial m^{(n)}(\boldsymbol{x}')} = g^{(n)}(\omega,r;\boldsymbol{x}') \; \Upsilon^{(n)}_m(\omega,\boldsymbol{x}') \; g^{(n)}(\omega,\boldsymbol{x}';e), \tag{14}$$

where $g(\omega, \boldsymbol{x}'; e)$ is the Green's function at point $\boldsymbol{x}'$ and originated at $\boldsymbol{x}_e$, and $g(\omega, r; \boldsymbol{x}')$ is the Green's function at point $\boldsymbol{x}_r$ and originated at $\boldsymbol{x}'$. Also,

$$\Upsilon_m^{(n)}(\omega, \boldsymbol{x}') = \Upsilon_c^{(n)}(\omega, \boldsymbol{x}') \frac{\partial c(\boldsymbol{x}')}{\partial m(\boldsymbol{x}')} = \omega c^{(n)}(\boldsymbol{x}') \tilde{k}^{(n)}(\boldsymbol{x}') \tag{15}$$

where $\tilde{k}^{(n)}$ satisfies (5) for $c^{(n)}$ and α. Note that α has been assumed fixed, and is thus not changed with n. The reader is referred to reference [3], section 4.1, for further details about derivation of (14). The minimisation problem (12) is equivalent to solving the linear equation

$$\nabla \mathcal{F}^{(n)}(\boldsymbol{x}) + \int H^{(n)}(\boldsymbol{x}, \boldsymbol{x}') \ \delta m(\boldsymbol{x}') \ d\boldsymbol{x}' = 0. \tag{16}$$

Here, the first term in the left-hand side is the functional gradient, which is weighted in data space (ω, r, e) and solution space $\boldsymbol{x}$, and is in the form

$$\nabla \mathcal{F}^{(n)}(\boldsymbol{x}) = \sum_{e,r} \int \mathcal{Q}_m^{(n)}(\boldsymbol{x}) \ \Big(\frac{\partial g^{(n)}(\omega, r; e)}{\partial m^{(n)}(\boldsymbol{x})} \Big)^* \ \mathcal{Q}_g^{(n)}(\omega, r; e) \ \delta g_{res}^{(n)}(\omega, r; e) \ d\omega. \tag{17}$$

Also, the second term, which is the action of the Hessian weighted in data and solution spaces, on the perturbation, yields [3]

$$H^{(n)}(\boldsymbol{x}) \ \delta m = \sum_{e,r} \int \mathcal{Q}_m^{(n)}(\boldsymbol{x}) \ \Big(\frac{\partial g^{(n)}(\omega, r; e)}{\partial m^{(n)}(\boldsymbol{x})} \Big)^* \ \mathcal{Q}_g^{(n)}(\omega, r; e) \ \delta g_{(\omega,r;e)}^{(n)}(\delta m) \ d\omega. \tag{18}$$

Here, $H^{(n)}(\boldsymbol{x})\delta m = \int H^{(n)}(\boldsymbol{x}, \boldsymbol{x}')\delta m(\boldsymbol{x}') \ d\boldsymbol{x}'$, where from (13) and (14),

$$\delta g_{(\omega,r;e)}^{(n)}(\delta m) = \int g^{(n)}(\omega, r; \boldsymbol{x}') \ \Upsilon_m^{(n)}(\omega, \boldsymbol{x}') \delta m(\boldsymbol{x}') \ g^{(n)}(\omega, \boldsymbol{x}'; e) \ d\boldsymbol{x}'. \tag{19}$$

Also, $\Upsilon_m^{(n)}(\omega, \boldsymbol{x}') \ \delta m(\boldsymbol{x}')$ is the complex scattering potential at point $\boldsymbol{x}'$. By plugging (9) into (18), the weighted Hessian can be written in the explicit form

$$H^{(n)}(\boldsymbol{x}, \boldsymbol{x}') = \sum_{e,r} \int \mathcal{Q}^{(n)}(\omega, r, e, \boldsymbol{x}) \ \mathcal{D}^{(n)}(\omega, r, e, \boldsymbol{x}, \boldsymbol{x}') \ e^{-i\Phi^{(n)}(\omega,r,e,\boldsymbol{x},\boldsymbol{x}')} \ d\omega, \tag{20}$$

where

$$\mathcal{Q}^{(n)}(\omega, r, e, \boldsymbol{x}) = \mathcal{Q}_m^{(n)}(\boldsymbol{x}) \mathcal{Q}_g^{(n)}(\omega, r, e). \tag{21}$$

Also,

$$\begin{aligned} \mathcal{D}^{(n)}(\omega, r, e, \boldsymbol{x}, \boldsymbol{x}') = \Big(A^{(n)}(\omega, r; \boldsymbol{x}) \Upsilon_m^{(n)}(\omega, \boldsymbol{x}) \ A^{(n)}(\omega, \boldsymbol{x}; e) \ \Big)^* \\ \Big(A^{(n)}(\omega, r; \boldsymbol{x}') \ \Upsilon_m^{(n)}(\omega, \boldsymbol{x}') \ A^{(n)}(\omega, \boldsymbol{x}'; e) \Big), \end{aligned} \tag{22}$$

and

$$\begin{aligned} \Phi^{(n)}(\omega, r, e, \boldsymbol{x}, \boldsymbol{x}') = \phi^{(n)}(\omega, r; \boldsymbol{x}) + \phi^{(n)}(\omega, \boldsymbol{x}; e) \\ - \left(\phi(\omega, r; \boldsymbol{x}') + \phi(\omega, \boldsymbol{x}'; e) \right). \end{aligned} \tag{23}$$

Now, the following two approximations are enforced on (20) [32, 35, 36, 37].

$$\mathcal{D}^{(n)}(\omega, r, e, \boldsymbol{x}, \boldsymbol{x}') \approx \mathcal{D}^{(n)}(\omega, r, e, \boldsymbol{x}', \boldsymbol{x}') \tag{24}$$

and

$$\begin{aligned}\Phi^{(n)}(\omega,r,e,\boldsymbol{x},\boldsymbol{x}') &\approx \nabla_{\boldsymbol{x}'}\left(\phi^{(n)}(\omega,r;\boldsymbol{x}')+\phi^{(n)}(\omega,\boldsymbol{x}';e)\right)\cdot(\boldsymbol{x}-\boldsymbol{x}')\\ &= \bar{\mathbf{k}}^{(n)}(\omega,r,\boldsymbol{x}';e)\cdot(\boldsymbol{x}-\boldsymbol{x}').\end{aligned} \tag{25}$$

Here, $\bar{\mathbf{k}}(\cdot,r,\boldsymbol{x}';e)$ is the gradient of the two-way isochron, the curve in the space of the scattering point $\boldsymbol{x}'$ on which the sum of accumulated phase from $\boldsymbol{x}_e$ to the scatterer $\boldsymbol{x}'$ and from the scatterer $\boldsymbol{x}'$ to $\boldsymbol{x}_r$ is equal [35, 36]. The notation $\cdot$ implies the dependence on ω for brevity, and will be applied from now on. $\bar{\mathbf{k}}(\cdot,r,\boldsymbol{x}';e)$ is thus a vector passing through $\boldsymbol{x}'$, normal to the two-way isochron, where $\bar{\mathbf{k}}(\cdot,r,\boldsymbol{x}';e)=\boldsymbol{k}_{(\cdot,\boldsymbol{x}';\boldsymbol{x}_e)}+\boldsymbol{k}_{(\cdot,\boldsymbol{x}_r;\boldsymbol{x}')}=\boldsymbol{k}_{(\cdot,\boldsymbol{x}';\boldsymbol{x}_e)}-\boldsymbol{k}_{(\cdot,\boldsymbol{x}';\boldsymbol{x}_r)}$ with $\boldsymbol{k}_{(\cdot,\boldsymbol{x}';\boldsymbol{x}_e)}$ (resp. $\boldsymbol{k}_{(\cdot,\boldsymbol{x}';\boldsymbol{x}_r)}$) the wavevector of the ray initialised at $\boldsymbol{x}_e$ (resp. $\boldsymbol{x}_r$) at point $\boldsymbol{x}'$.

For sufficiently smooth wavenumber k, the contribution of e and r to the Hessian $H(\boldsymbol{x},\boldsymbol{x}')$ oscillates by moving far away from a ray linking the emitter-receiver pair (e,r) along the planes perpendicular to the ray and vanishes everywhere except in some vicinity of the ray. By moving far away from the linked ray, $\Phi^{(n)}(\omega,r,e,\boldsymbol{x},\boldsymbol{x}')$ increases and $\mathcal{D}^{(n)}(\omega,r,e,\boldsymbol{x},\boldsymbol{x}')$ decreases, and therefore the contribution of e and r to the Hessian decays. In ray theory, for any emission point e and reception point r, the volume around a ray linking e and r that contributes into the wavefield at r has been widely studied, and is termed *Fresnel volume*. A point $\boldsymbol{x}$ belongs to the Fresnel volume corresponding to a linked ray (e,r) at frequency ω, if and only if the discrepancy of the accumulated phase on the ray linking e to r and the two-way accumulated phase from e to $\boldsymbol{x}$ and $\boldsymbol{x}$ to r be smaller than one half the wavelength, i.e.,

$$|\phi(\omega,r;\boldsymbol{x})+\phi(\omega,\boldsymbol{x};e)-\phi(\omega,r;e)|<\pi. \tag{26}$$

For further details, the reader is referred to reference [33], section 3.1.6. By assuming that rays do not have any caustics, only points which are sufficiently close to the ray linking e and r satisfy (26). The approximation (25) implies that for any pair of points $\boldsymbol{x}$ and $\boldsymbol{x}'$ with sufficiently small $|\phi(\omega,r;\boldsymbol{x})+\phi(\omega,\boldsymbol{x};e)-\phi(\omega,r;e)|$, the two-way accumulated phase associated with $\boldsymbol{x}$ can be approximated using a Taylor-series expansion to the two-way accumulated phase associated with $\boldsymbol{x}'$, for which the second and higher order terms are neglected. In addition, the approximation (24) assumes that for any pair of points $\boldsymbol{x}$ and $\boldsymbol{x}'$ in some vicinity of the ray linking e and r,

$$A(\cdot,r;\boldsymbol{x})\Upsilon_m(\cdot,\boldsymbol{x})\;A(\cdot,\boldsymbol{x};e)\approx A(\cdot,r;\boldsymbol{x}')\;\Upsilon_m(\cdot,\boldsymbol{x}')\;A(\cdot,\boldsymbol{x}';e). \tag{27}$$

This approximation is based on two assumptions. Firstly, in some vicinity of a linked ray (e,r) that contributes into the Hessian, the changes in the two-way attenuation from e to r are ignored. Secondly, considering (15), it was assumed that the variations in $\alpha_0 c\omega^{(y-1)}$ throughout the medium is much smaller than 1. For example, for soft tissues like the breast, the sound speed 1500 ms^{-1}, $\alpha_0=0.5$ $\mathrm{dBMHz}^{-y}\mathrm{cm}^{-1}$ (equivalent to 1.75×10^{-9} $\mathrm{Np(rad/s)}^{-y}\mathrm{m}^{-1}$), and frequency 1MHz, will give $\alpha_0 c\omega^{(y-1)}\approx 1.375\times10^{-3}\mathrm{Np/rad}$.

Now, by plugging the approximations (24) and (25) into (20), the Hessian operator is reduced to the form

$$\begin{aligned}H^{(n)}(\boldsymbol{x},\boldsymbol{x}') &= \sum_{e,r}\int \mathcal{Q}^{(n)}(\omega,r,e,\boldsymbol{x})\;e^{-i\bar{\mathbf{k}}^{(n)}(\omega,r,\boldsymbol{x}';e)\cdot(\boldsymbol{x}-\boldsymbol{x}')}\;\mathcal{D}^{(n)}(\omega,r,e,\boldsymbol{x}',\boldsymbol{x}')\;d\omega\\ &= \iiint \frac{1}{\Delta e\;\Delta r}\mathcal{Q}^{(n)}(\omega,r,e,\boldsymbol{x})\;e^{-i\bar{\mathbf{k}}^{(n)}(\omega,r,\boldsymbol{x}';e)\cdot(\boldsymbol{x}-\boldsymbol{x}')}\;\mathcal{D}^{(n)}(\omega,r,e,\boldsymbol{x}',\boldsymbol{x}')\;d\omega\;dr\;de.\end{aligned} \tag{28}$$

Now, by assuming that rays do not have caustics or any other singularities, the variables of integration are changed using a one-to-one map $(\omega,r,e)\to(|\bar{\mathbf{k}}|,\zeta,\theta)$. Here, on each arbitrary point $\boldsymbol{x}$,

and emitter-receiver pair (e, r), θ is defined as the scattering angle, and satisfies

$$\theta(\cdot, r, \boldsymbol{x}'; e) = \gamma_r(\cdot, \boldsymbol{x}') + \pi - \gamma_e(\cdot, \boldsymbol{x}'), \tag{29}$$

where γ_e and γ_r are the angle of the wavevector of rays initialised at $\boldsymbol{x}_e$ and $\boldsymbol{x}_r$, respectively. Also, the pair $(|\bar{\mathbf{k}}|, \zeta)$ is a polar representation of the two-way wavevector $\bar{\mathbf{k}}(\cdot, r, \boldsymbol{x}'; e)$, which is normal to the two-way isochron $\boldsymbol{x}_e \to \boldsymbol{x}' \to \boldsymbol{x}_r$. Here, the angle of the two-way wavevector $\zeta(\cdot, r, \boldsymbol{x}'; e)$ satisfies

$$\zeta(\cdot, r, \boldsymbol{x}'; e) = \frac{1}{2}(\gamma_e(\cdot, \boldsymbol{x}') + \gamma_r(\cdot, \boldsymbol{x}') + \pi), \tag{30}$$

and the magnitude satisfies

$$|\bar{\mathbf{k}}| = 2\ k\ \cos(\frac{\theta}{2}). \tag{31}$$

Now, applying the change of variables $(\omega, r, e) \to (|\bar{\mathbf{k}}|, \zeta, \theta)$ on (28) yields

$$\begin{aligned} H^{(n)}(\boldsymbol{x}, \boldsymbol{x}') = \iiint \frac{1}{\Delta e\ \Delta r}\ \mathcal{Q}^{(n)}(\omega, r, e, \boldsymbol{x})\ e^{-i\bar{\mathbf{k}}^{(n)}(\omega, r, \boldsymbol{x}'; e)\cdot(\boldsymbol{x}-\boldsymbol{x}')} \times \\ \mathcal{D}^{(n)}(\omega, r, e, \boldsymbol{x}', \boldsymbol{x}') \left| \frac{\partial(\omega, r, e)}{\partial(|\bar{\mathbf{k}}|, \zeta, \theta)} \right|\ d|\bar{\mathbf{k}}|\ d\zeta\ d\theta, \end{aligned} \tag{32}$$

where $\times$ is a multiplication operator for scalars. Following [32, 35, 36, 37], we now choose $\mathcal{Q}^{(n)}$ such that $H^{(n)}(\boldsymbol{x}, \boldsymbol{x}')$ be diagonalised and can thus be inverted in a single step. Accordingly, by choosing

$$\mathcal{Q}^{(n)}(\omega, r, e, \boldsymbol{x}) = \frac{\Delta e \Delta r}{(2\pi)^2} \frac{|\bar{\mathbf{k}}^{(n)}(\omega, r, \boldsymbol{x}; e)|}{\mathcal{D}^{(n)}(\omega, r, e, \boldsymbol{x}, \boldsymbol{x})} \left| \frac{\partial(|\bar{\mathbf{k}}|, \zeta, \theta)}{\partial(\omega, r, e)} \right|, \tag{33}$$

the Hessian operator in (28) collapses to

$$H(\boldsymbol{x}, \boldsymbol{x}') = \int \Big(\frac{1}{(2\pi)^2} \iint |\bar{\mathbf{k}}| e^{-i\bar{\mathbf{k}}(\boldsymbol{x}')\cdot(\boldsymbol{x}-\boldsymbol{x}')}\ d|\bar{\mathbf{k}}| d\zeta \Big)\ d\theta \approx 2\pi\delta(\boldsymbol{x} - \boldsymbol{x}'). \tag{34}$$

Here, we used the fact that the term inside the parenthesis in (34) can be expressed as a sampled (in angular and wavenumber domains) and band-limited variant of the exact Fourier transform of the delta function in the cylindrical coordinates [35], i.e.,

$$\frac{1}{(2\pi)^2} \int_{\zeta=0}^{2\pi} \int_{-\infty}^{+\infty} |\bar{\mathbf{k}}| e^{-i\bar{\mathbf{k}}(\boldsymbol{x}')\cdot(\boldsymbol{x}-\boldsymbol{x}')}\ d|\bar{\mathbf{k}}|\ d\zeta = \delta(\boldsymbol{x} - \boldsymbol{x}'). \tag{35}$$

In addition, the Jacobian determinant included in the weighting function (33) gives

$$\left| \frac{\partial(|\bar{\mathbf{k}}|, \zeta, \theta)}{\partial(\omega, r, e)} \right| = \left| \frac{\partial(|\bar{\mathbf{k}}|)}{\partial\omega} \right| \left| \frac{\partial\gamma_e}{\partial e} \right| \left| \frac{\partial\gamma_r}{\partial r} \right|, \tag{36}$$

where

$$\left| \frac{\partial(|\bar{\mathbf{k}}(\boldsymbol{x})|)}{\partial\omega} \right| = 2\cos\Big(\frac{\theta(\boldsymbol{x})}{2}\Big) \Big[\frac{1}{c(\boldsymbol{x})} + y\tan(\frac{\pi y}{2}) \omega^{(y-1)}\ \alpha_0(\boldsymbol{x}) \Big]. \tag{37}$$

Now, considering (21) and by plugging the weighting function in (33) into the functional gradient (17), and then plugging (17) into the linearised equation (16), together with using (34), give a search direction

$$\delta m^{(n)}(\boldsymbol{x}') \approx \Re \left\{ \sum_{e,r,\omega} \Lambda^{(n)}(\omega, r, e, \boldsymbol{x}')\ \delta g_{res}(m^{(n)}; \omega, r; e) \right\}. \tag{38}$$

Here, $\Re\{\cdot\}$ denotes the real part, and

$$\Lambda^{(n)}(\omega, r, e, \boldsymbol{x}') = \frac{\Delta e \Delta r \Delta \omega}{(2\pi)^3} \left|\frac{\partial \gamma_e^{(n)}(\omega, \boldsymbol{x}')}{\partial e}\right| \left|\frac{\partial \gamma_r^{(n)}(\omega, \boldsymbol{x}')}{\partial r}\right| \left|\frac{\partial |\bar{\mathbf{k}}(\omega, r, \boldsymbol{x}'; e)|}{\partial \omega}\right| \times |\bar{\mathbf{k}}^{(n)}(\omega, r, \boldsymbol{x}'; e)| \big(\Upsilon_m^{(n)}(\omega, \boldsymbol{x}')\big)^{-1} g_\dagger^{(n)}(\omega, \boldsymbol{x}'; e)\ g_\dagger^{(n)}(\omega, \boldsymbol{x}'; r), \tag{39}$$

where

$$g_\dagger^{(n)}(\omega, \boldsymbol{x}; \boldsymbol{x}') = \frac{\exp\big(-i(\phi^{(n)}(\omega, \boldsymbol{x}; \boldsymbol{x}') + \pi/4)\big)}{A^{(n)}(\omega, \boldsymbol{x}; \boldsymbol{x}')}. \tag{40}$$

Here, $g_\dagger$ is termed *reversed* Green's function, where $\dagger$ indicates that the Green's function is reversed in both phase and amplitude. Note also that in $g_\dagger^{(n)}(\omega, \boldsymbol{x}'; r)$, which acts on $\delta g_{res}(m^{(n)}; \omega, r; e)$, the reciprocity of Green's function has been used [47]. In addition, in Eq. (39), the parameters $|\partial\gamma_e/\partial e|\Delta e$ and $|\partial\gamma_r/\partial r|\Delta r$ are approximated using finite differences

$$\left|\frac{\partial \gamma_e(\boldsymbol{x}')}{\partial e}\right| \Delta e \approx \frac{1}{2}|\gamma_{(e+1)}(\boldsymbol{x}') - \gamma_{(e-1)}(\boldsymbol{x}')| \tag{41}$$

and

$$\left|\frac{\partial \gamma_r(\boldsymbol{x}')}{\partial r}\right| \Delta r \approx \frac{1}{2}|\gamma_{(r+1)}(\boldsymbol{x}') - \gamma_{(r-1)}(\boldsymbol{x}')|, \tag{42}$$

where the subscript $\gamma_{(e\pm1)}$ (resp. $\gamma_{(r\pm1)}$) denotes the adjacent emitters (resp. receivers).
The backprojection operator in Eq. (39) corrects for the decay in amplitude and shift in phase of the scattered waves via reversing the incident and scattering Green's functions. The factors $|\partial\gamma_e/\partial e|\Delta e$ and $|\partial\gamma_r/\partial r|\Delta r$ correct for the nonuniformity and sparsity of the angles the emitters and receivers are seen by any scattering point in the medium, respectively. In addition, the Born approximation is based on a low-frequency assumption, and assumes that the waves originated at emitter e and measured by receiver r can be affected by scattering at any points in the medium. Instead, the backprojection operator derived in Eq. (39) implies that the high-frequency waves dominate the scattered waves. The correction factors accounting for the scattering angles in $|\bar{\mathbf{k}}||\partial\bar{\mathbf{k}}/\partial\omega|$ makes an assumption that for the waves originated at emitter e, the scatterers in some vicinity of a ray linking the emitter-receiver pair (e, r) will affect the scattered waves on receiver r more likely than scatterers far way from the linked ray. This high-frequency assumption agrees with the assumption of smoothness of the wavenumber map $k^{(n)}$ that was used in the two approximations (24) and (25), because the smoothness assumption is more accurate at high frequencies.
Finally, the update of the squared slowness is computed using $m^{(n+1)} = m^{(n)} + \tau\ \delta m^{(n)}$, where τ is the step length, which is fixed for all n. The updates $c^{(n)}$ can then be obtained from $m^{(n)}$.

4. Ray tracing

This section describes a numerical implementation of the method described above for implementing UST. Specifically, this section explains how the ray theory based on a high frequency approximation is used for computing the terms in the approximate Green's function and its reversed variant for heterogeneous and absorbing media. In general, rays are curves that are perpendicular to surfaces of constant phase, i.e., they are tangent to the wavevector $\boldsymbol{k}$, which satisfies

$$\boldsymbol{k} = \nabla\phi, \tag{43}$$

and therefore the eikonal equation

$$\nabla\phi \cdot \nabla\phi = k^2. \tag{44}$$

The eikonal equation can be expressed in the form of a Hamiltonian

$$H(\boldsymbol{x},\boldsymbol{k}) = \frac{1}{2}k^{-1}\left(\boldsymbol{k}\cdot\boldsymbol{k} - k^2\right), \tag{45}$$

where we recall that k is the real part of $\tilde{k}$, and is dependent on c through Eq. (5). The Hamiltonian yields $H = 0$ along a reference ray satisfying the canonical equations

$$\begin{aligned} \dot{\boldsymbol{x}} &= \nabla_{\boldsymbol{k}} H \\ \dot{\boldsymbol{k}} &= -\nabla_{\boldsymbol{x}} H. \end{aligned} \tag{46}$$

For each emitter-receiver pair (e, r), the canonical vector of the reference ray is introduced as $\boldsymbol{y}(s) = \left[\boldsymbol{x}(s), \boldsymbol{k}(s)\right]^T$, where s is the arc length on the ray, and T is the transpose operator. Here, the initial position of the reference ray matches the position of the emitter and has an arc length s_0, i.e., $\boldsymbol{x}(s_0) = \boldsymbol{x}_e$, and the initial wavevector $\boldsymbol{k}(s_0)$ is chosen such that the reference ray is intercepted by the receiver r after travelling through the medium. This is done through ray linking, which will be explained at the end of this section. Further details about how the rays are sampled in terms of the arc length, s, are given in the next section.

The contributions of the amplitude factor A in Eq. (9) from the geometrical spreading is A_{geom}, and is determined by how the area of the ray tube changes compared to a reference point on the ray, and relies on the concept of the ray Jacobian [33]. In [3], the ray Jacobian was defined by the rate at which two closely-spaced rays diverge, and was computed for each linked ray using finite differences. (cf. [33], section 3.10.4.3.) Computing the ray Jacobian using finite differences requires at least two additional auxiliary rays for each linked ray (or emitter-receiver pair) in 2D. Here, the ray Jacobian is computed using *paraxial* ray tracing, also known as *dynamic* ray tracing. Instead of tracing auxiliary rays independent of the reference ray, paraxial ray tracing involves solving an additional system of linear ordinary differential equations for tracing paraxial ray, which can be solved simultaneously with the ray tracing system for the reference ray. (cf. [33], section 3.10.4.4.) For each emitter-receiver pair, the paraxial ray is traced along a reference ray which has been computed through ray linking, i.e., a reference ray which links the corresponding emitter-receiver pair.

Accordingly, a paraxial ray is defined by the first-order approximation $\boldsymbol{y}(s) + \delta\boldsymbol{y}(s)$, where $\delta\boldsymbol{y}(s) = \left[\delta\boldsymbol{x}(s), \delta\boldsymbol{k}(s)\right]^T$ is the perturbation to the canonical vector of the reference ray, and satisfies the paraxial ray tracing system of equations

$$\delta\dot{\boldsymbol{y}} = \mathbf{D}\ \delta\boldsymbol{y}, \tag{47}$$

where

$$\mathbf{D} = \begin{bmatrix} \nabla_{\boldsymbol{x}}\nabla_{\boldsymbol{k}} H & \nabla_{\boldsymbol{k}}\nabla_{\boldsymbol{k}} H \\ -\nabla_{\boldsymbol{x}}\nabla_{\boldsymbol{x}} H & -\nabla_{\boldsymbol{k}}\nabla_{\boldsymbol{x}} H \end{bmatrix}. \tag{48}$$

Using the ray equations (46), the unit vector $d\boldsymbol{x}/ds$ and the wavevector $\boldsymbol{k}$ satisfy the ray equations

$$\frac{d\boldsymbol{x}}{ds} = k^{-1}\boldsymbol{k}, \qquad \frac{d\boldsymbol{k}}{ds} = \frac{1}{2}\nabla k(k^{-2}\boldsymbol{k}\cdot\boldsymbol{k} + 1), \tag{49}$$

where we remind that $k^{-2}|\boldsymbol{k}|^2 = 1$ for $H = 0$.

Also, using (47) and (48), the paraxial ray equations are in the form

$$\begin{aligned} \frac{d}{ds}\delta\boldsymbol{x} &= (-k^{-2}\nabla k\boldsymbol{k}^T)\ \delta\boldsymbol{x} + (k^{-1})\ \delta\boldsymbol{k} \\ \frac{d}{ds}\delta\boldsymbol{k} &= (\nabla^2 k - k^{-1}\nabla k\nabla k^T)\ \delta\boldsymbol{x} + (k^{-2}\boldsymbol{k}\nabla k^T)\ \delta\boldsymbol{k}. \end{aligned} \tag{50}$$

Here, the paraxial ray tracing system defined by (49) and (50) is numerically implemented using a second-order variant of Runge-Kutta (RK) scheme, known as Heun's method, which provides a good compromise between accuracy and speed [48, 49]. An outline of the Heun's approach for solving the paraxial ray tracing system is given in Algorithm 1.
The system (47) is a ray, if the perturbation vector $\delta \boldsymbol{y}$ satisfies

$$\delta H = \nabla_{\boldsymbol{k}} H \cdot \delta \boldsymbol{k} + \nabla_{\boldsymbol{x}} H \cdot \delta \boldsymbol{x} = 0. \tag{51}$$

In addition, considering (49), δH is constant along any solutions of the paraxial system, so it is sufficient to ensure the condition (51) at the initial point [50].
Initial conditions: The initial wavevector is specified by the frequency ω, the sound speed in water c_0 and the initial unit vector. Following [3], the rays are initialised at $\boldsymbol{x}_e$ and are connected to $\boldsymbol{x}_r$ through ray linking [38]. Ray-linking is in class of shooting methods, and seeks to find a ray trajectory which provides the stationary path within a family of neighborhood paths between $\boldsymbol{x}_e$ and $\boldsymbol{x}_r$ by enforcing a boundary condition on the rays' path such that the ray initialised at position of emitter e is intercepted by the receiver r after travelling across the medium. For each iteration (linear subproblem) of the UST inverse problem, and emitter–receiver pair (e, r), ray linking is performed by iteratively determining the initial unit direction of the ray initialised from the emitter e using an optimisation algorithm such that the interception point of the ray by the detection surface (ring) matches the position of the receiver r within a tolerance [33, 51]. Having determined the initial wavevector $\boldsymbol{k}(s_0)$ and using the condition (51), together with enforcing the constraint $\delta \boldsymbol{x}(s_0) = 0$, the initial perturbation to the wavevector $\delta \boldsymbol{k}(s_0)$ must satisfy $\boldsymbol{k}(s_0) \cdot \delta \boldsymbol{k}(s_0) = 0$.
Grid-to-ray interpolation: The squared slowness map is updated on the grid points, so for implementing algorithm 1, it must be interpolated onto the rays' sampled points. Here, the grid-to-ray interpolation was performed using a B-spline interpolation, which provides continuous values for ∇k and $\nabla^2 k$ at any arbitrary (offgrid) point. (For further details, see [3].)
Ray-to-grid interpolation: The parameters of the Green's function on the grid points are computed by interpolation from the linked rays onto the grid points using a trilinear interpolation [3].

5. Ray coordinates

This section describes how the reversed Green's function is approximated and discretised along the linked rays. The formulae are derived for $g_\dagger(\cdot, \boldsymbol{x}; e)$, but they can also be applied for $g_\dagger(\cdot, \boldsymbol{x}; r)$ after interchanging e and r. In general, for the 2D case, the coordinates of the ray are given by two parameters: one specifying the initial direction (angle) of the ray and another a monotonic parameter along the ray [33]. Here, the ray parameters are chosen the initial angle, θ, and the arc length, s.

Definition 1. The trajectory of a ray linking an emission point e to a reception point r is defined by the sampled arc lengths $s_i,\ i \in \left\{0, ..., M_{(e,r)}\right\}$. Therefore, the sampled points are initialised at s_0 with $\boldsymbol{x}(s_0) := \boldsymbol{x}_e$, and are terminated at $s_{M_{(e,r)}}$ with $\boldsymbol{x}(s_{M_{(e,r)}}) := \boldsymbol{x}_r$, the position of receiver r. The sampled arc length s_i satisfy

$$s_i = \begin{cases} i\Delta s, & i \in \left\{0, ..., M_{(e,r)} - 1\right\} \\ (i-1)\,\Delta s + \Delta s', & i = M_{(e,r)}. \end{cases} \tag{52}$$

Here, the second line is used in order to indicate that the last point of the ray must be matched to the reception point r, and therefore $\Delta s' = s_{M_{(e,r)}} - s_{M_{(e,r)-1}}$ with $\Delta s' \leqslant \Delta s$ [38].

Algorithm 1 Paraxial ray tracing for the linked ray using Heun's method

input: $\boldsymbol{x}_e$, $k := k(\boldsymbol{x})$ ▷ Input initial ray position and wavenumber
initialise: $\boldsymbol{x}, \boldsymbol{k}$ ▷ Set initial position, and compute the initial wavevector through ray linking
$\delta\boldsymbol{x} = 0,\ \delta\boldsymbol{k}$ satisfying $\delta\boldsymbol{k} \cdot \boldsymbol{k} = 0,$ ▷ Set initial conditions: paraxial ray (amplitude)
while $\boldsymbol{x}(s)$ is inside Ω **do**

$- - -$ ▷ **Update the reference ray**
$\boldsymbol{k} \leftarrow k\ \boldsymbol{k}/\mid \boldsymbol{k} \mid$ ▷ Normalise the ray direction
$q_{\boldsymbol{x}} = \boldsymbol{k}/k$ ▷ Compute the update variables
$q_{\boldsymbol{k}} = \nabla k(\boldsymbol{x})$
$\boldsymbol{k}' \leftarrow \boldsymbol{k} + \Delta s\ q_{\boldsymbol{k}}$ ▷ Update the auxiliary ray direction
$k' \leftarrow k(\boldsymbol{x} + \Delta s\ q_{\boldsymbol{x}})$ ▷ Update the auxiliary wavenumber
$\boldsymbol{k}' \leftarrow k'\boldsymbol{k}'/\mid \boldsymbol{k}' \mid$ ▷ Normalise the auxiliary ray direction
$q'_{\boldsymbol{x}} = \boldsymbol{k}'/k'$ ▷ Compute the auxiliary update variables
$q'_{\boldsymbol{k}} = \nabla k(\boldsymbol{x} + \Delta s\ q_{\boldsymbol{x}})$
$\boldsymbol{x} \leftarrow \boldsymbol{x} + \Delta s(q_{\boldsymbol{x}} + q'_{\boldsymbol{x}})/|q_{\boldsymbol{x}} + q'_{\boldsymbol{x}}|$ ▷ Update the ray position
$\boldsymbol{k} \leftarrow \boldsymbol{k} + (\Delta s/2)(q_{\boldsymbol{k}} + q'_{\boldsymbol{k}})$ ▷ Update the ray direction

$- - -$ ▷ **Update the paraxial ray: amplitude**
$q_{\delta\boldsymbol{x}} = (-\nabla k\boldsymbol{k}^T/k^2)\delta\boldsymbol{x} + (1/k)\delta\boldsymbol{k}$ ▷ Compute the update variables
$q_{\delta\boldsymbol{k}} = \Big(\nabla^2 k - \nabla k\nabla k^T/k\Big)\delta\boldsymbol{x} + (\boldsymbol{k}\nabla k^T/k^2)\delta\boldsymbol{k}$
$\delta\boldsymbol{k}' \leftarrow \delta\boldsymbol{k} + \Delta s\ q_{\delta\boldsymbol{k}}$ ▷ Update the auxiliary ray direction perturbation
$\delta\boldsymbol{x}' \leftarrow \delta\boldsymbol{x} + \Delta s q_{\delta\boldsymbol{x}}$ ▷ Update the auxiliary ray position perturbation
$q'_{\delta\boldsymbol{x}} = (-\nabla k'\boldsymbol{k}'^T/k'^2)\delta\boldsymbol{x}' + (1/k')\delta\boldsymbol{k}'$ ▷ Compute the auxiliary update variables
$q'_{\delta\boldsymbol{k}} = \Big(\nabla^2 k' - \nabla k'\nabla k'^T/k'\Big)\delta\boldsymbol{x}' + (\boldsymbol{k}'\nabla k'^T/k'^2)\delta\boldsymbol{k}'$
$\delta\boldsymbol{x} \leftarrow \delta\boldsymbol{x} + (\Delta s/2)(q_{\delta\boldsymbol{x}} + q'_{\delta\boldsymbol{x}})$ ▷ Update the ray position perturbation
$\delta\boldsymbol{k} \leftarrow \delta\boldsymbol{k} + (\Delta s/2)(q_{\delta\boldsymbol{k}} + q'_{\delta\boldsymbol{k}})$ ▷ Update the ray direction perturbation

end while

Definition 2. For each excitation e, the parameters of the Green's function is approximated on a set of linked rays $f_{(k,r;e)} = 0$. These rays are parameterised in space as $\boldsymbol{x}(s_i, \theta_{(r,e)})$, which denotes the position on the arc length s of the point i along a ray linking the emission position $\boldsymbol{x}_e$ to the reception position $\boldsymbol{x}_r$. Also, the polar initial direction of this ray is indicated by $\theta_{(r,e)}$.

Accordingly, the reversed Green's function $g_\dagger(\cdot, \boldsymbol{x}; \boldsymbol{x}_e)$ is discretised on the sampled points along the rays linking the emitter e to all receivers r using the coordinates defined in Definition 2 in the form

$$g_\dagger\big(\cdot, \boldsymbol{x}(s_i, \theta_{(r,e)}); e\big) \approx \frac{\exp\Big(-i\big(\phi(\cdot, \boldsymbol{x}(s_i, \theta_{(r,e)}); e) + \pi/4\big)\Big)}{A\big(\cdot, \boldsymbol{x}(s_i, \theta_{(r,e)}); e\big)}, \tag{53}$$

where $\boldsymbol{x}_e := \boldsymbol{x}(s_0, \theta_{(r,e)})$ for all r. (cf. Eq. (40).) In (53), the accumulated phase ϕ is approximated in the form

$$\phi(\cdot, \boldsymbol{x}(s_i, \theta_{(r,e)}); e) = \int_{s_0}^{s_i} k(\boldsymbol{x}(s_i, \theta_{(r,e)}))\ ds - \frac{\pi}{2}\mathcal{K}(s_i, \theta(r, e)), \tag{54}$$

where $\mathcal{K}(s_i, \theta(r, e))$ is the cumulative times the sign of the ray Jacobian along the ray has been changed. Points on which the ray Jacobian changes sign are called *caustics*, and will lead to a $\pi/2$ shift in the phase [33].

The contributions of the amplitude factor A from absorption, A_{abs}, is computed in the form

$$A_{abs}(\cdot, \boldsymbol{x}(s_i, \theta_{(r,e)}); e) = \exp\left(-\int_{s_0}^{s_i} \alpha(\boldsymbol{x}(s_i, \theta_{(r,e)}))\ ds\right). \tag{55}$$

The contributions of the amplitude factor A from the geometrical spreading, A_{geom}, is determined by the relative change of the ray Jacobian along the ray with respect to a reference point on which the amplitude can be determined analytically [52]. Correspondingly, the Jacobian J on the point i along the ray initialised by angle $\theta_{(r,e)}$ satisfies

$$J(s_i, \theta_{(r,e)}) = \det\, \Xi(s_i, \theta_{(r,e)}), \tag{56}$$

where Ξ is the *transformation matrix* from the ray coordinates $\gamma = \left[\gamma_1, \gamma_2\right]^T$ to the general Cartesian coordinates $\boldsymbol{x} = \left[\boldsymbol{x}_1, \boldsymbol{x}_2\right]^T$, and is in the form $\Xi = \partial x/\partial\gamma$.

In general, γ_1 must be a parameter specifying the ray, and γ_2 must be a monotonic parameter along the ray. (See [33], section 3.10.) Here, $\gamma_1 = \theta$ and $\gamma_2 = s$, as discussed in Definition 2. The geometrical attenuation A_{geom} now satisfies

$$A_{\text{geom}}(\cdot, \boldsymbol{x}(s_i; \theta_{(r,e)}); e) = \left(\frac{c(\boldsymbol{x}(s_i, \theta_{(r,e)}))}{c(\boldsymbol{x}(s_1, \theta_{(r,e)}))}\frac{J(s_1, \theta_{(r,e)})}{J(s_i, \theta_{(r,e)})}\right)^{1/2} A_{\text{geom}}(\cdot, \boldsymbol{x}(s_1, \theta_{(r,e)}); e), \tag{57}$$

where s_1 is the arc length of the first sampled point after the initial point on the ray, and is chosen as the reference point, using an assumption that a neighborhood of the emitter points with a radius greater than ray spacing Δs is acoustically homogeneous, and therefore, $A_{\text{geom}}(\cdot, \boldsymbol{x}(s_1, \theta_{(r,e)}); e)$ can be calculated analytically [33].

6. Numerical results

This section describes numerical experiments demonstrating the effectiveness of the proposed ray-based inversion approach for a low-cost computation of a high-resolution image of the sound speed distribution inside the breast.

6.1. **Data simulation.** An imaging system consisting of 64 emitters and 256 receivers uniformly distributed along a circular ring with radius $R = 9.5$cm was simulated. A horizontal slice of a 3D digital phantom, which mimics the acoustic properties of the breast and is freely available [53], was used in this study. The sound speed was set to a range 1470–1580 ms^{-1}, and the absorption coefficient α_0 was set to a range 0–1 $\text{dBMHz}^{-y}\text{cm}^{-1}$, and the power law exponent y was set to 1.4. Figures 1(a) and 1(b) show the maps for the sound speed and absorption coefficient of the breast phantom, respectively. The sound speed and absorption coefficient in water was set 1500 ms^{-1} and 0, respectively. The computational grid consisted of 502×502 grid points with position $[-10.04, +10.00] \times [-10.04, +10.00]\text{cm}^2$ and a grid spacing of $\Delta x = 4 \times 10^{-2}$cm along all the Cartesian coordinates. Using this sound speed distribution and grid spacing, the maximum frequency supported by the grid, $f_{\max}$, was 1.84 MHz.

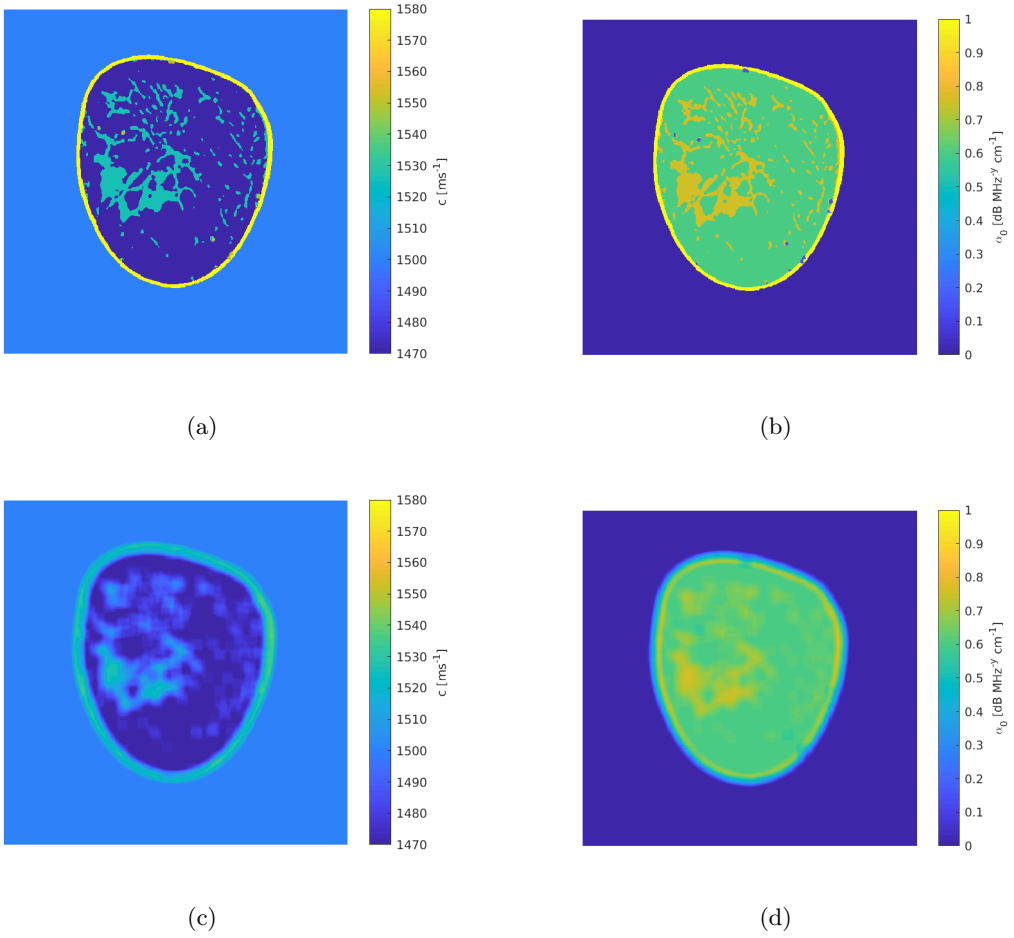

FIGURE 1. Phantom used for simulation of the synthetic UST data using the full-wave approach: (a) sound speed [ms^{-1}] (b) absorption coefficient [dB MHz^{-y}cm^{-1}], (c) smoothed sound speed [ms^{-1}], (d) smoothed absorption coefficient [dB MHz^{-y}cm^{-1}]. The maps are shown on a grid consisting of 502×502 points (used for the wave simulation). The maps (c) and (d) are smoothed by applying an averaging window of size 17 points on the original acoustic maps (a) and (b), respectively. The original (nonsmoothed) acoustic maps were used for simulating the data used for image reconstruction, and the smoothed maps were used for simulating the data used as a benchmark for comparison with the ray approximation to heteroegenous Green's function. The power law exponent was assumed $y = 1.4$ and homogeneous.

Simulating time series data. A corrected version of a *k-space pseudo-spectral* method for simulationg time-varying source was used to simulate the acoustic pressure time series data on the detection ring. This was done via solving a system of three-coupled first-order wave equations equivalent to the Szabo's second-order wave equation, which is a time-domain variant of Eq. (2) with the complex wavenumber defined by (5) [39, 40, 41, 42, 43]. The emitters and receivers were assumed as points placed on the circle, and the interpolation of the pressure field between the grid and

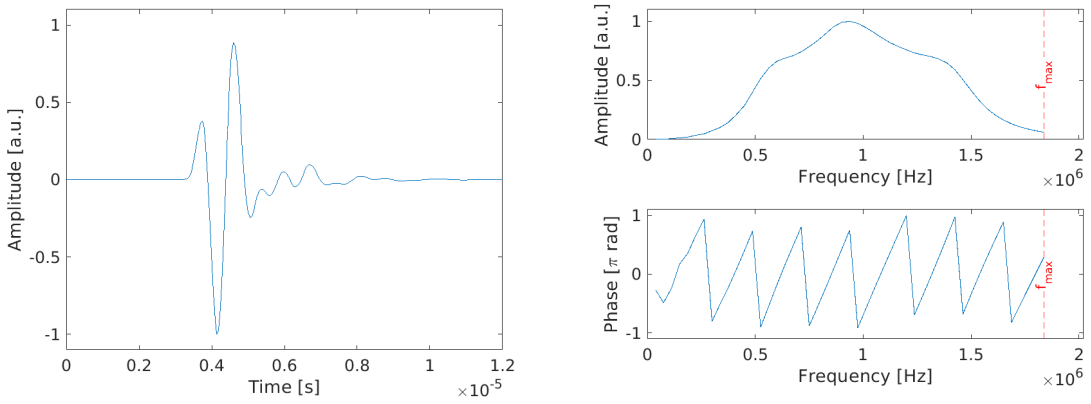

(a) (b)

FIGURE 2. Acoustic source used for all excitations (emitters): (a) time domain, (b) frequency domain: normalised amplitude and phase. f_{max} indicates the maximum frequency supported by the grid used for the wave simulations.

these transducers was performed using a Fourier approach [42]. To simulate the data, each emitter was individually driven by an excitation pulse, and the induced acoustic pressure time series were recorded at the receivers at 6466 time points with a sampling rate of 39.6MHz (25.25 ns time spacing). This was repeated for each emitter. Figure 2(a) shows the normalised amplitude of the acoustic source in the time domain, and figure 2(b) shows the normalised amplitude and phase components of the acoustic source in frequency domain, respectively. This signal is used as the acoustic source for all excitations.

6.2. **Numerical validation of the ray approximation to the Green's function.** In this section, the approximate Green's function solution to Szabo's wave equation is compared to a full-wave solution using the k-space pseudo-spectral method [40, 41, 42, 43] in a heterogeneous and absorbing medium with a spatially smooth variations in acoustic properties. It must be reminded that the approximate heterogeneous Green's function was introduced in section 2, and its numerical approximation and discretisation were explained in sections 4 and 5, respectively. Further details about derivation of the Green's function solution to Szabo's wave equation were given in [3]. For the full-wave approach, emitter 1 was excited by the acoustic pulse shown in figures 2(a) and 2(b), and the induced pressure propagated across the breast in water, and was recorded on all the 256 receivers. The Green's function $g(\omega, r; e)$ depends only on the accumulated parameters and geometrical spreading along the linked rays, and does not include the scattering effects. Therefore, for a fair comparison, the scattering effects were minimised in the full-wave simulation by applying an averaging window of size 17 grid points on the sound speed and absorption coefficient maps. The smoothed sound speed and absorption coefficient maps are shown in figures 1(c) and 1(d), respectively.

For the ray-approximation approach, the Green's function was approximated along the linked rays, and was then included in the Green's formula (7) in order to approximate the pressure time series on the receivers after an excitation of emitter 1. Note that in (7), the integral in space is dropped for a point source. In the image reconstruction below, the inverse crime was avoided by using two different computational grids for data simulation and image reconstruction. (Note that using

different grids may not be necessary in our study, because two inherently different approaches are used for the data simulation and image reconstruction.) For image reconstruction below, the computational grid has a size 204×204 points with a grid spacing of 1 mm. Therefore, the ray approximation to the Green's function used for comparison with the full-wave simulation was also performed on the same grid. For implementing the ray approximation to the Green's function, the smoothed sound speed and absorption coefficient maps used for the full-wave simulation were interpolated onto the grid for image reconstruction, and the interpolated wavenumber map was smoothed again by an averaging window of size 7 points in order to minimise interpolation effects. (Compared to the grid for full-wave simulation, the averaging window size was reduced reciprocally to the increase in the grid spacing.) The pressure field produced by emitter 1 was approximated on all the 256 receivers at a single frequency 1 MHz and for three cases: only water, non-absorbing breast and absorbing breast inside water.

Figure 3(a) shows the phase of the pressure time series on all the receivers after an excitation of emitter 1. (The phases were wrapped to $[-\pi, \pi]$.) The green plot shows the phases which are analytically computed by the homogeneous Green's function by assuming only water, and the red plot shows the phases computed using the ray approximation to the Greens function for the absorbing breast inside water. Also, the phase of the pressure time series simulated by the full-wave approach for the absorbing breast inside water was shown by the blue plot. As shown in this figure, for receivers in the range 50-180, for which the linked rays travel through the breast (not only water), the ray approximation to the heterogeneous and absorbing Green's function and the full-wave simulation have very good agreement, but the Green's function analytically calculated by assuming only water has large discrepancies with the full-wave simulation.

Figure 3(b) shows the amplitude of the pressure time series on all the receivers after an excitation of emitter 1. The green plot shows the amplitudes computed by the analytic Green's function assuming only water. The amplitudes computed using the Green's function assuming a nonabsorbing breast, i.e., the amplitudes attenuated by only the geometrical spreading, were approximated on all the receivers using (57), and are shown by the light blue plot. It must be reminded that for computing (57), the rays' Jacobian was approximated using paraxial ray tracing, as discussed in section 4. The amplitudes computed using the Green's function for the absorbing breast were approximated as the product of the amplitude decay because of geometrical spreading (the light blue plot) and the accumulated acoustic absorption, and are shown by the red plot. The accumulated acoustic absorption was computed using (55). The amplitudes of the pressure time series simulated by the full-wave approach and recorded on all the receivers are shown by the dark blue plot. As shown in this figure, for the absorbing breast, the amplitudes computed by the product of the geometrical spreading using paraxial ray tracing and the accumulated acoustic absorption have very good agreement with the amplitudes computed by the full-wave simulation, but the analytically calculated Green's function assuming only water or the Green's function neglecting the acoustic absorption have large discrepancies with the full-wave simulation.

6.3. **Image reconstruction.** This section explains the procedure for image reconstruction from the simulated ultrasound data using the full-wave approach, and shows the reconstructed images. A corrected version [43] of the k-Wave [42] (Version 1.3) for simulating time-varying source was used for simulating two sets of synthetic data, as described in section 6.1. The first data set was simulated for only water, and the second data set was simulated for the digital breast phantom inside water. The breast-in-water data was simulated using the sound speed and absorption coefficient maps shown in figures 1(a) and 1(b), respectively. For simulating each data set, each emitter was sequentially excited by the excitation pulse shown in figures 2(a) and 2(b), and the induced

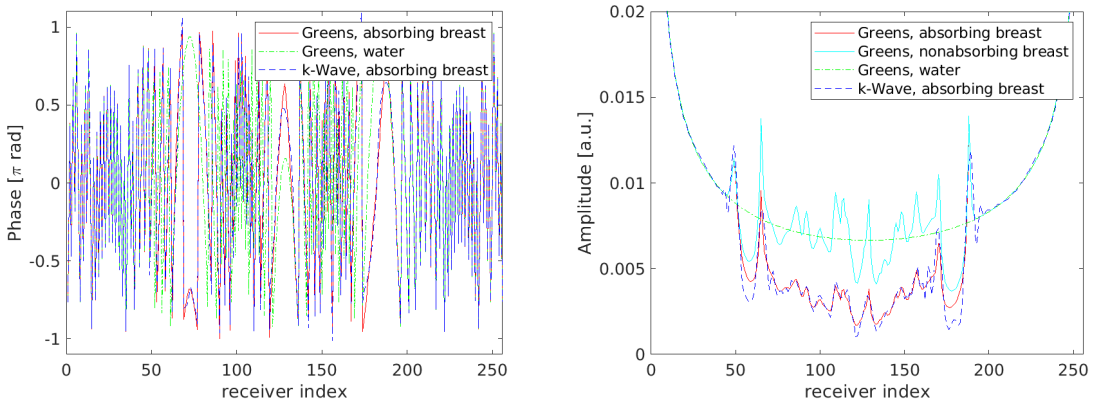

FIGURE 3. The pressure time series on all the receivers at single frequency 1 MHz after an excitation of emitter 1: (a) phase, (b) amplitude.

pressure time series were recorded on all the receivers in time. The excitation and measurements were sequentially repeated for all the emitters. The computational time for simulation of the UST data set including all the excitations for the digital breast phantom inside water using the k-Wave's Matlab code [42] on a single 8-core Xeon E5-2620 v4 2.1 GHz CPU was about 5 hours. Different levels of additive white Gaussian noise (AWGN) were added to the simulated pressure time series to provide 40 dB, 30 dB and 25 dB signal-to-noise ratio (SNR) of the peak amplitudes for both breast-in-water and only-water data sets.

For reducing an inverse crime in time spacing, the time series simulated by the full-wave approach on the receivers were temporally downsampled by 2 before image reconstruction. Also, the grid for image reconstruction consisted of 204×204 grid points with position $[-10.1650, +10.1350] \times [-10.1650, +10.1350]\text{cm}^2$ and a grid spacing of $\Delta x = 1\text{mm}$ along all the Cartesian coordinates. The image reconstruction was performed on the grid points inside a binary mask with radius 0.95 of the radius of the detection ring. Because the sound speed is reconstructed on the grid points, the parameters of the reversed Green's function, which are approximated on the linked rays, must be interpolated onto the grid points. The interpolation of the approximated parameters of the reversed Green's function on the linked rays onto the grid points were done by enforcing a triangulation on the sampled points on the linked rays and using a trilinear interpolation. The reversed Green's functions $g_\dagger(\omega, \boldsymbol{x}; r)$ were computed by reversing the accumulated parameters on the linked rays associated with the reversed Green's functions $g_\dagger(\omega, \boldsymbol{x}; e)$ [3]. Note that for approximating the geometrical portion of the amplitudes for $g_\dagger(\omega, \boldsymbol{x}; r)$, an additional paraxial ray must be traced along each reversed ray.

6.3.1. *Inversion approach using time-of-flights (initial guess).* Because the objective function in (10) is highly nonlinear, an initial guess is often used [12, 13, 14, 16]. Here, an image reconstruction approach based on the direct time of flight (TOF) of the measured (simulated) pressure time series was used to provide an initial guess. The TOF-based inversion approach iteratively minimises the norm of discrepancy between the TOFs obtained from the measured (simulated) pressure time series using a first-arrival picking algorithm [11] and the TOFs modelled by the ray tracing algorithm. The effects of measurement errors on the picked first-arrivals are compensated

for using a difference inversion approach, in which the difference of the sound speed of the breast in water and only water is computed from the discrepancy of the first-arrival times picked from the measured breast-in-water and only-water data sets. The minimisation is performed by iteratively linearising the associated objective function, and solving the arising linearised subproblems using a Radon-type technique. Here, each linearised subproblem was solved using a Simultaneous Algebraic Reconstruction Technique (SART) algorithm, which accounts for the nonuniform ray density across the image due to the curved nature of the rays [55]. For computing rays' trajectories at each linearisation, the sound speed update was smoothed by an averaging window of size 7 grid points, but integration of accumulated time-of-flights along trajectory of the linked rays was performed on the nonsmooth updates, i.e., the constructed system matrix was multiplied by the nonsmoothed sound speed update. The ray linking was performed using the Secant method such that for each emitter-receiver pair, the linked ray (the optimal ray after ray linking) for each linerisation is used as the initial guess for ray linking for the next linearisation [38, 3]. The TOF-based algorithm was terminated after few linearisations to provide a good trade-off between accuracy and the artefact due to the error in the picked first-arrival times [3].

6.3.2. *Inversion approaches using ray approximation to heterogeneous Green's function.* Below, the procedure for implementing the inversion approach based on the Green's function is explained. For evaluating the effectiveness of the proposed inversion approach, the approach used in [3] was used as the benchmark. The image reconstruction is determining the squared slowness map, m, which minimises the objective function (10). The inverse problem is solved via discretising the objective function at a number of frequencies within the frequency range of the transducers, and linearisation and minimisation of the objective function from low to high frequencies until the computed update direction for the linearised subproblem associated with a frequency set becomes smaller than a tolerance. For computing the residual (11), the measured Green's function $\hat{g}_{(\omega,r;e)}$ is derived by deconvolving the excitation pulse from the measured (simulated) pressure time series. Here, the deconvolution was performed using a Tikhonov regularised inversion approach in the frequency domain [54]. Also, the Green's functions $g_{(m;\omega,r;e)}$ were approximated along the linked rays computed on the last update of the sound speed.

Ray linking. For the TOF-based and the Green's function-based approaches, the ray linking was performed on the updates of the sound speed and wavenumber maps for each of emitter-receiver pairs separately. For each update of the wavenumber map and each emitter-receiver pair, the ray linking was done by iteratively updating the initial unit direction of the ray using a Secant method [3, 38, 51]. The initial guess for the unknown initial unit direction of the ray was set the obtained optimal initial direction after ray linking for the last previous update of the wavenumber map, and the ray's trajectory was iteratively computed using the first part of Algorithm 1 until the interception point of the ray by the detection ring matches the position of the reception point within a tolerance. The parameters of Green's functions g (included in the residual) and $g_\dagger$ (included in the backprojection formula) were then computed along the linked rays. (See the formulae given in section 5 for $g_\dagger$.) For computing the geometrical portion of the amplitude, the linked ray is used as the reference ray, and a paraxial ray is computed via implementing the second part of Algorithm 1. For ray tracing, an averaging window of size 7 grid points was applied on the updated wavenumber maps, but the nonsmoothed updates were used for integration along the rays and approximating the Green's functions using the formulae in section 5.

a) Hessian-inversion-free ray-born inversion. The inversion approach described in section 3 was implemented at 140 discretised frequencies in the range $f \in \{0.2, ..., 1.5\}$MHz. The image reconstruction was performed from low to high frequencies such that each update of the squared slowness

map was computed at two consecutive discretised frequencies using Eq. 38. ($n \in \{1, ..., 75\}$.) For each linearisation n, the Green's functions, $g(\omega; r; e)$, included in the residual and the reversed Green's functions, $g_\dagger(\omega, \boldsymbol{x}; e)$ and $g_\dagger(\omega, \boldsymbol{x}; r)$, which are included in the backprojection formula (39), were computed on the forward and backward rays, the rays which are initialised on emitters e and receivers r, respectively. The step length was heuristically chosen $\tau = 1.2 \times 10^{-1}$ for all linearisations. The major portion of the computational cost for solving each linear problem (16) is ray tracing, because the update direction is obtained in one step using (38). Therefore, using this inversion approach, the computational cost for solving each linearised subproblem is almost the same as each linearised subproblem in the TOF-based algorithm. Note that the total number of linearisations required for reaching an optimal point using this approach was almost five to ten times more than the TOF-based algorithm.

b) Hessian-inversion-based ray-born inversion (Gauss-Newton). Using $\mathcal{Q} = I$, where I is an identity matrix, in the linearised subproblem (12), each arising linearised subproblem n (16) is solved by first forming the gradient $\nabla \mathcal{F}^{(n)}$ and then computing the update direction via iteratively computing the action of the Hessian matrix $H^{(n)}$ on the updates of perturbation to the squared slowness map. This is equivalent to computing a Gauss-Newton search direction. The reader is referred to [3] for further details. Here, each linearised subproblem was solved using 10-15 inner iterations. Note that early stopping the inner iterations has regularising effects on the solution. In order to provide a benchmark for evaluating performance of the proposed Hessian-inversion-free ray-born inversion algorithm, the Gauss-Newton inversion approach described in [3] was implemented at 100 discretised frequencies in the range $f \in \{0.2, ..., 1.1\}$MHz. Like the Hessian-inversion-free approach, the image reconstruction was performed from low to high frequencies such that each update of the sound speed was computed at two consecutive discretised frequencies. ($n \in \{1, ..., 50\}$.) Compared to the Hessian-inversion-free approach, the algorithm was terminated at smaller n, because solving linearised subproblems at frequencies larger than 1.1 MHz provided very small search directions. Note that as described in section 4, the geometrical portion of the amplitude was computed via solving a paraxial system of equations, not auxiliary rays, as done in [3]. (cf. Algorithm 1.) The step length was heuristically chosen $\tau = 3 \times 10^4$ for all linearisations. Using our developed code in a Matlab environment and using the CPU mentioned in the first paragraph in section 6.3, the computational time for solving each linearised subproblem n and computing each Gauss-Newton search direction was almost an order of magnitude more than solving each linearised subproblem using the proposed Hessian-inversion-free approach. Compared to the full-wave inversion, the total computational time for reconstructing an image using the Gauss-Newton algorithm was almost the same as the computational time for simulating the breast-in-water UST data using k-Wave, i.e., solving a single forward problem using the corrected full-wave approach [42, 43]. As described in section 3, the sound speed images c can then be reconstructed from the updates of the squared slowness maps m.

6.4. **Reconstructed images.** In this section, the sound speed images reconstructed using the proposed Hessian-inversion-free ray-born inversion approach are shown, and are compared to the images reconstructed using the Gauss-Newton inversion approach [3]. The reconstructed images are evaluated in terms of Relative Error (RE), i.e.,

$$RE_{\text{image}} = \frac{\|c_{\text{image}} - c_{\text{phantom}}\|_2}{\|c_{\text{water}} - c_{\text{phantom}}\|_2} \times 100, \tag{58}$$

where c_{phantom} and c_{image} are the stack-vectors of the sound speed of the digital breast phantom interpolated onto the grid for image reconstruction and the reconstructed sound speed image, respectively. These stack-vectors were obtained on the grid points inside the binary mask for image

reconstruction. Also, the speed of sound in water has been assumed $c_{\text{water}} = 1500$ ms^{-1}. (cf. section 6.1.)

6.4.1. *Reconstructed images from UST data with high SNR.* Below, the reconstructed sound speed images from the synthetic ultrasound data with a high signal-to-noise ratio (SNR) are shown, and are evaluated in terms of RE. Figure 4(a) shows the sound speed map of the digital breast phantom (ground truth). Figure 4(b) shows the image reconstructed from time-of-flights of the time-series with 40 dB SNR. The time-of-flights were computed using a modified Akaike-Information-Criterion (AIC) approach [11].
As described in section 2, the proposed forward model based on the ray approximation to heterogeneous Green's function can account for the acoustic absorption and dispersion, but the absorption coefficient α_0 map and the exponent power y are not known in a practical setting. Here, the exponent power was assumed known and set $y = 1.4$, and the image reconstruction was performed using three assumptions: known α_0 map (figure 1(b)), zero α_0, and a homogeneous α_0 which can be determined in a practical setting from the mean logarithmic relative amplitudes of the measured time series for the only-water to the breast-in-water data sets. (Here, the homogeneous absorption coefficient was set 0.5 dBMHz^{-y}cm^{-1}.)
Figures 4(c) and 4(d) show the reconstructed sound speed images from the 40 dB-SNR synthetic ultrasound data using an assumption that α_0 map is known and using the Gauss-Newton and the proposed Hessian-inversion-free ray-born inversion approaches, respectively. In the same way, figures 4(e) and 4(f) show the reconstructed images using the assumption that α_0 is zero everywhere, i.e., the acoustic absorption and dispersion are neglected. Also, figures 4(g) and 4(h) show the reconstructed images assuming the homogeneous absorption coefficient $\alpha_0 = 0.5$ dBMHz^{-y}cm^{-1} inside the breast. The RE of the reconstructed images are written in the caption of the figure.
As shown in these figures for the high-SNR UST data used in this experiment, the images reconstructed using the Gauss-Newton inversion approach, which is based on an implicit and iterative inversion of the full Hessian matrix, are more accurate than those reconstructed by the Hessian-inversion-free approach in terms of RE. Furthermore, an assumption of zero α_0 has led to less accuracy and more artefact for the reconstructed images, but assuming homogeneous α_0 for the breast has provided images almost the same as those reconstructed using an assumption of true and known α_0 in terms of RE. It must be reminded that the exponent power was assumed known for both cases.

6.4.2. *Reconstructed images from UST data with medium and low SNR.* Below, the reconstructed images from simulated ultrasound data with medium and low SNR and using an assumption of homogeneous $\alpha_0 = 0.5$ dBMHz^{-y}cm^{-1} are presented. Accordingly, figures 5(a) and 5(b) show the TOF-based images computed from the UST synthetic data with 30 dB and 25 dB SNR, respectively. Figures 5(c) and 5(d) show the images reconstructed using the Gauss-Newton inversion approach and from the UST data with 30 dB and 25 dB SNR, respectively. In the same way, figures 5(e) and 5(f) show the images reconstructed using the proposed Hessian-inversion-free approach. As shown in figures 5(a)-5(d), an increase in the additive white Gaussian noise in the UST data have led to more artefact and greater RE in the TOF-based reconstructed images (initial guesses) and the images reconstructed using the Gauss-Newton inversion approach. Additionally, figures 5(e) and 5(f) show that the proposed Hessian-inversion-free ray-born inversion approach has reconstructed images with less artefact than the Gauss-Newton inversion approach from the UST data with 30 dB and 25 dB SNR. For the data with 25 dB SNR, the sound speed image reconstructed using the Hessian-inversion free approach is more accurate than the Gauss-Newton approach in terms of RE.

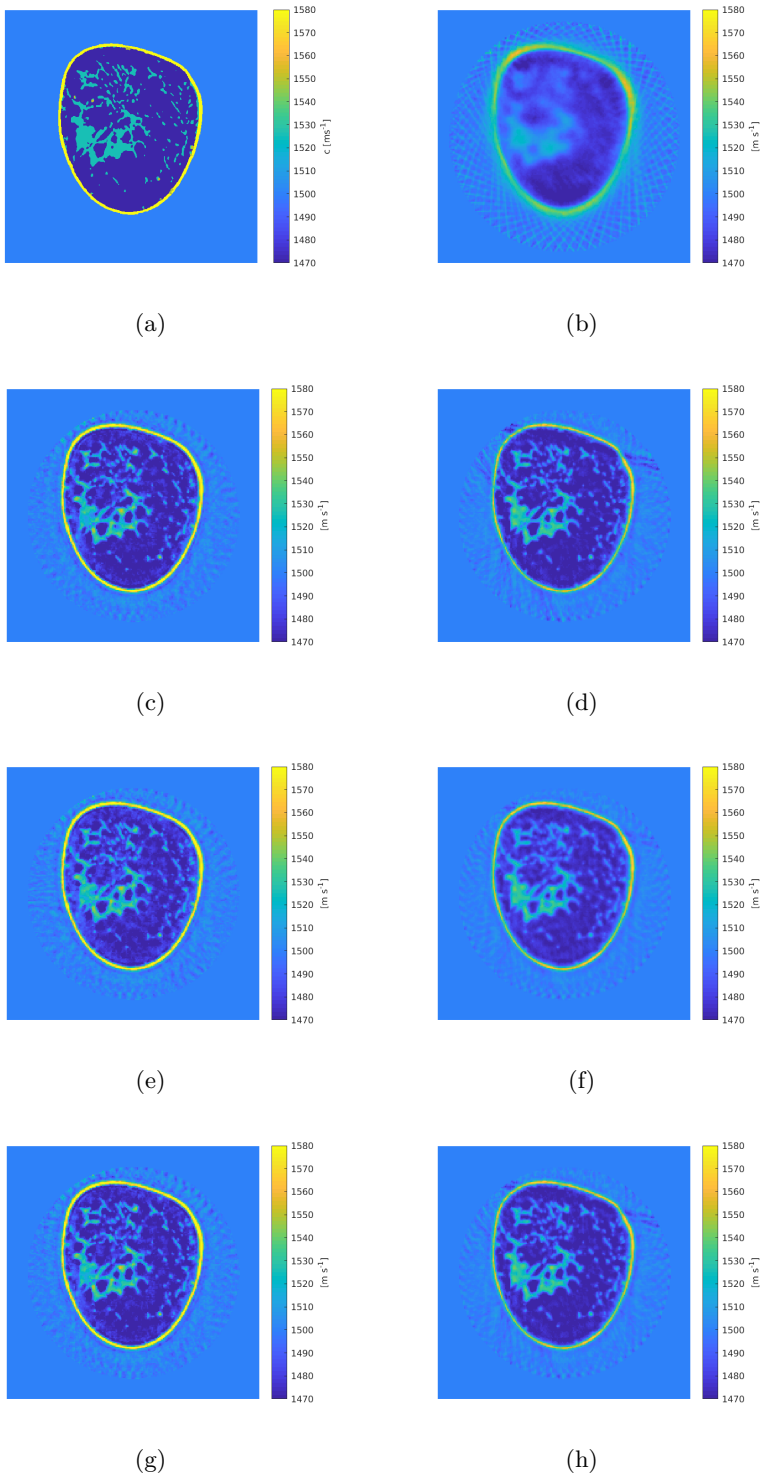

FIGURE 4. (a) Ground truth. Reconstructed sound speed images from UST data with 40dB SNR: (b) time-of-flight-based approach (initial guess), $RE = 73.52\%$. True α_0 (Figure 1(b)): (c) Gauss-Newton, $RE = 38.92\%$, (d) Hessian-inversion-free, $RE = 44.76\%$. $\alpha_0 = 0$: (e) Gauss-Newton, $RE = 41.01\%$, (f) Hessian-inversion-free, $RE = 47.85\%$. $\alpha_0 = 0.5$ dBMHz^{-y}cm^{-1} (homogeneous inside breast): (g) Gauss-Newton, $RE = 39.55\%$, (h) Hessian-inversion-free, $RE = 44.45\%$.

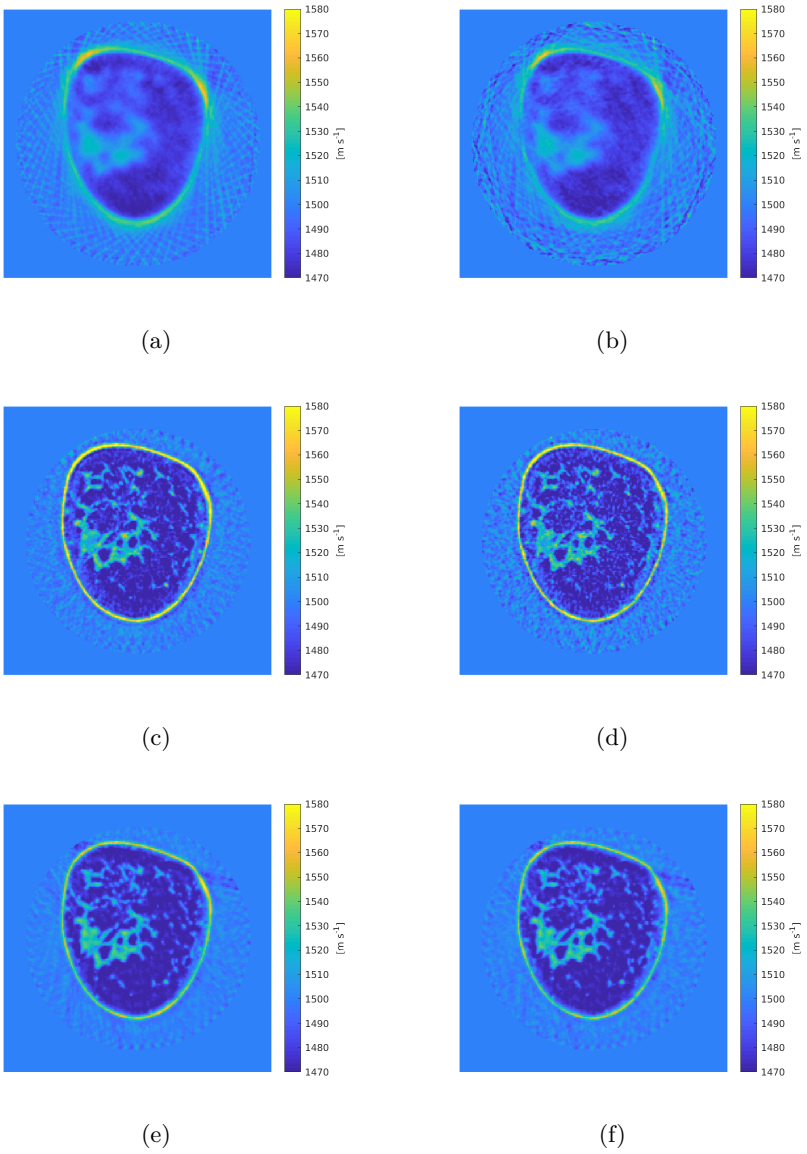

FIGURE 5. Reconstructed images using Time-of-flight-based approach (initial guess): (a) 30 dB, $RE = 76.56\%$, (b) 25 dB, $RE = 81.82\%$, Gauss-Newton: (c) 30 dB, $RE = 45.50\%$, (d) 25 dB, $RE = 53.76\%$, Hessian-inversion-free: (e) 30 dB, $RE = 47.13\%$, (f) 25 dB, $RE = 48.93\%$. The absorption coefficient map of the breast was assumed homogeneous and $\alpha_0 = 0.5$ dBMHz^{-y}cm^{-1}.

Figures 6(a), 6(b) and 6(c) show the reconstructed quantities of the sound speed on the main diagonal of the grid for image reconstruction from UST data with 40 dB, 30 dB and 25 dB SNR, respectively. The quantities of the sound speed for the digital breast phantom, which was interpolated from the grid for the k-Wave simulation onto the grid for image reconstruction, are shown by the black colour. In addition, the quantities obtained using the TOF-based approach

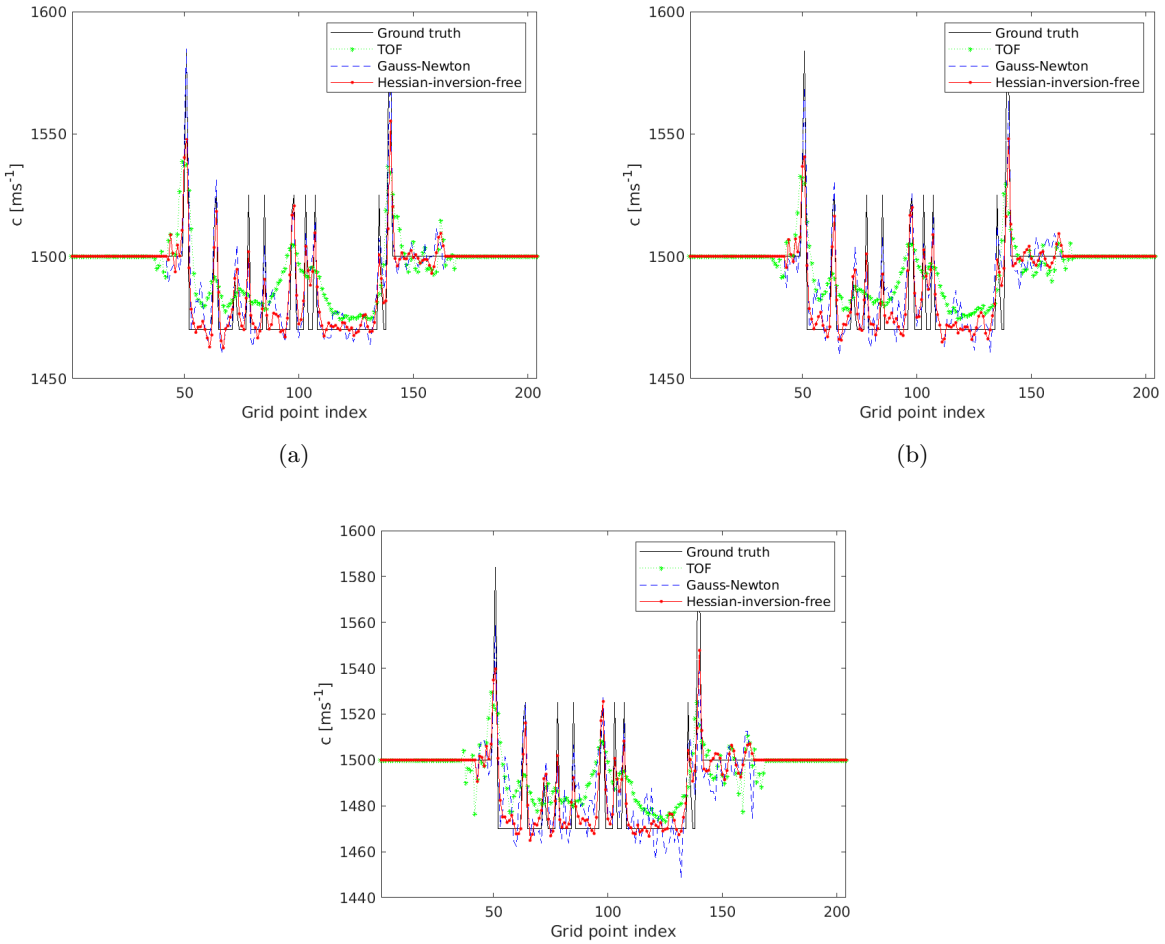

FIGURE 6. The reconstructed quantities of the sound speed on the main diagonal of the grid for image reconstruction from ultrasound data with: a) 40 dB SNR, b) 30 dB SNR, and c) 25 dB SNR. The absorption coefficient map of the breast was assumed homogeneous and $\alpha_0 = 0.5$ dBMHz^{-y}cm^{-1}.

are shown by the green colour, and the quantities reconstructed using the Gauss-Newton and the proposed Hessian-inversion-free approaches are shown by the blue and red colours, respectively. As shown in these figures, the contrast level of the sound speed map reconstructed using the Hessian-inversion-free approach is slightly smaller than the Gauss-Newton approach, but the quantities reconstructed using the Hessian-inversion-free approach were more stable to noise in data than the Gauss-Newton approach. Note that the computational cost of the proposed Hessian-inversion-free inversion approach is almost an order of magnitude less than the Gauss-Newton approach.

7. DISCUSSION

This paper proposed an efficient approach for quantitative reconstruction of the sound speed from ultrasound time series. It was shown that this inversion approach can reconstruct an image of the

sound speed distribution of soft tissues accurately. Here, the performance of this approach was tested on a digital breast phantom [53]. Using this inversion approach, the propagation of acoustic waves is modelled based on Green's formula in which aberrations in the phase and amplitude of the Green's function because of heterogeneity, refraction, geometrical spreading, and acoustic absorption and dispersion, are accounted for. For approximating the amplitude decay because of geometrical spreading, the changes in the area of ray tube is computed for each linked ray via solving a paraxial system of equations using Algorithm 1, as described in section 4. The proposed ray-based inversion approach reconstructed a high-resolution image of the breast phantom via including the first-scattered waves in the image reconstruction. It is expected that a great portion of the higher-scattered waves are attenuated because of acoustic absorption, and are buried in noise in a practical setting. The proposed inversion approach is different from other Born and distorted Born inversion approaches used for medical UST, because these approaches neglect the heterogeneity of the medium in modelling the Green's function, and include the heterogeneity only in the scattering potential [22, 23, 24, 25, 40, 27, 29, 30]. However, figures 3(a) and 3(b) show that neglecting the acoustic heterogeneity in computing the Green's function has led to large errors in approximating phase and amplitude, respectively.

For solving the inverse problem, it was shown that the total computational cost of the Gauss-Newton inversion approach, which solves each linear subproblem via an implicit and iterative inversion of the Hessian matrix, was almost the same as the computational time for simulating the breast-in-water synthetic data set using the corrected full-wave approach [42, 43], i.e., solving single forward problem of the full-wave inversion. Furthermore, the proposed Hessian-inversion-free inversion approach was computationally about an order of magnitude faster than the Gauss-Newton inversion approach, because the linear subproblem associated with each frequency set is solved in a single step using (38) and (39). In addition, the proposed Hessian-inversion-free ray-born inversion approach was more stable than the Gauss-Newton approach to noise. For UST data with 30 dB and 25 dB SNR, the proposed Hessian-inversion-free inversion approach reconstructed sound speed images with lower artefact than the Gauss-Newton inversion approach. Moreover, the proposed Hessian-inversion-free approach was more stable than the Gauss-Newton approach to changes in the parameters of the image reconstruction or the initial guess.

The proposed forward model accounts for acoustic absorption and dispersion via solving a lossy Helmholtz equation based on Szabo's wave equation, but the map of acoustic absorption coefficient is not known in a practical setting. It was shown that images reconstructed using an assumption of homogeneous absorption coefficient is comparable to the images reconstructed using a true and known absorption coefficient map for the breast, but neglecting absorption has led to less accurate reconstructed images.

In general, ray-born inversion approaches combine ray theory with Born approximation. The latter, which is based on a low-frequency approximation, assumes that the scattered waves measured on receivers can be affected by the scattering at any point in the medium. However, the inversion approach proposed in this study uses a high frequency approximation, and dominates the scattered waves along a ray linking the associated emitter-receiver pair. While this assumption is not exact, it is a very good approximation for the frequency ranges used in the prototype ultrasound systems [4, 9].

In addition, the diagonalisation of the Hessian matrix is based on an assumption of an exact 2D Fourier integral of the Dirac delta function. However, because of partial coverage of $\bar{\mathbf{k}}$ in the polar coordinates $|\bar{\mathbf{k}}|$ and ζ, the Fourier integral derived via weighting the Hessian matrix is not exact. The coverage of $\bar{\mathbf{k}}$ is partial, because firstly the transducers are band-limited and secondly their distribution on the ring is sparse. Therefore, because of the filtering enforced on the derived 2D

Fourier integral in polar coordinates of $\bar{\mathbf{k}}$, the resulting Hessian matrix is actually a Dirac delta function which has been smoothed in space. As shown in the line plots in figures 6(a), 6(b) and 6(c), the filtered Fourier integral has led to slight smoothness and loss of contrast in the reconstructed images, but it significantly improved the stability of image reconstruction against noise in data, changes in the parameters of image reconstruction and initial guess. (The two latter were not shown.) The hope is that the spatial resolution and the contrast of images reconstructed using the Hessian-inversion-free approach be improved via using closely-spaced and broadband transducers.

Data and code availability statement

The Matlab codes that support the findings of this study, as well as studies [3] and [38], are publicly available via the GitHub link in [1]. The original k-Wave simulated ultrasound data, which were used as the benchmark for findings of this study can either be reproduced via the example scripts in [1], or downloaded via the Zenodo link in [2] and added to the associated path in the GitHub project.

Acknowledgement

The author would like to thank the anonymous reviewers of this manuscript in the journal of *Inverse Problems* for useful comments for improving the quality of this work. The author apologises to the reviewers if their potential feedbacks for this manuscript (the first revised version) have not been applied, because the reviews and the last decision of the associated editor have not been shared with the author yet, and the author is not aware of the status of the submitted revision. Contacting the journal and IOP publishing (in London) did not help understanding the status of this paper.

Appendix-A. A correction to the k-Wave for simulation of the time-varying source [43]

A k-space method for solving the coupled first-order differential equations for propagation of acoustic waves in heterogeneous media was proposed in [41]. As discussed in section 6, an open-source toolbox for a numerical implementation of this approach was used in this study for simulating the UST pressure data recorded on the receivers, but some steps for inclusion of time-varying source have been corrected. For example, Eq. (2.19) in the k-Wave user manual [56], or equivalently Algorithm 1, line 5, the second term in the right-hand-side in [57], which have been used for arbitrary number of dimensions, were not understood. (See `kspaceFirstOrder_scaleSourceTerms.m` in the k-Wave Version 1.3.) Here, the corrected procedure taken for simulation of a time-varying source using the k-Wave is explained for lossless medium. (An inclusion of the acoustic absorption and dispersion in the simulation is straightforward.) To simulate acoustic waves for a lossless medium with d dimensions ($d \in \{2, 3\}$), the coupled first-order partial differential equations should be defined in terms of the source $s(\boldsymbol{x}, t)$ in the form

$$\begin{aligned} \frac{\partial}{\partial t}\boldsymbol{u}(\boldsymbol{x}, t) &= -\frac{1}{\rho_0}\nabla p(\boldsymbol{x}, t) \\ \frac{\partial}{\partial t}\boldsymbol{\rho}(\boldsymbol{x}, t) &= -\rho_0 \nabla \boldsymbol{u}(\boldsymbol{x}, t) + \int_0^t s(\boldsymbol{x}, t')\ dt' \\ p(\boldsymbol{x}, t) &= c(\boldsymbol{x})^2 \boldsymbol{\rho}(\boldsymbol{x}, t), \end{aligned} \tag{59}$$

where p is the scalar acoustic pressure in $\mathrm{kgm}^{2-d}\mathrm{s}^{-2}$, and $\boldsymbol{\rho}$ and $\boldsymbol{u}$ denote the vectors of acoustic density and particle velocity, respectively. Also, ρ_0 is the ambient density and is assumed homogeneous. In (59), an assumption $\int_0^{T_s} s(\boldsymbol{x}, t)\ dt = 0$ has been used. The second term in the

right-hand-side of the second line represents the mass source s_M, which is the time rate of the input of mass per unit volume in units of $\mathrm{kgm}^{-d}\mathrm{s}^{-1}$, and satisfies

$$s(\boldsymbol{x}, t) = \frac{\partial s_M(\boldsymbol{x}, t)}{\partial t}. \tag{60}$$

Numerical Implementation. Here, compared to the k-Wave toolbox, two corrections were applied. Firstly, Eq. (60) has been neglected in the k-Wave. Secondly, the dimension-dependent factor $1/(\Delta x)^d$ for spatial sampling of the Dirac delta function has been missed, where Δx is the grid spacing, and is assumed the same for all dimensions here [43]. In other words, according to Eq. (2.19) in the k-Wave manual [56], the current form of the relation between the discretised source $s(\boldsymbol{X}, n)$ (*source.p*) and the directional components of the mass source $s_M(\boldsymbol{X}, n)$ in the k-Wave is in the form

$$s_M^i(\boldsymbol{X}, n) = \frac{2s(\boldsymbol{X}, n)}{c_0 \; d \; \Delta x}, \tag{61}$$

but it must be in the form

$$s_M^i(\boldsymbol{X}, n) = \frac{\Delta t}{d} \sum_{n'=1}^{n} s(\boldsymbol{X}, n'), \tag{62}$$

where s is in units of $\mathrm{kgm}^{-d}\mathrm{s}^{-2}$, and s_M^i denotes the isotropic mass source along the coordinate i. Also, $\boldsymbol{X}$ and n denote the discretised space and time, respectively. In addition, Δt is the time spacing. Note that the factor $1/d$ in both Eqs. (61) and (62) takes into account that at each time iteration n, the isotropic source S_M is added to the d components of the acoustic density vector $\boldsymbol{\rho}$ separately. In addition, in an ideal case when a point source is positioned on a point $\boldsymbol{x}_0$ which matches the discretised position $\boldsymbol{X}_0$ on the grid, the discretised form of a point source gives

$$s(\boldsymbol{x})\delta(\boldsymbol{x} - \boldsymbol{x}_0) \equiv \frac{1}{(\Delta x)^d} s(\boldsymbol{X}_0), \tag{63}$$

where the dependence on time has been neglected for brevity. Here, the factor $1/(\Delta x)^d$ has been enforced as a scaling factor on the amplitude of the point source to account for the spatial sampling. The readers are referred to [3] (figure 3) to see the agreement between the homogeneous Green's function and the modified implementation of the k-Wave using (62) and (63). The same agreements have been obtained for the 3D homogeneous medium. To see the agreements in a smoothly varying heterogeneous medium, the readers are referred to [3] and figures 3(a) and 3(b) in this manuscript. Using the k-Wave Version 1.3 used for simulating propagation of a time-varying source $s(\boldsymbol{x}, t)$, a replacement of (62) and (63) by (61) is equivalent to taking a temporal integration from the excitation pulse and multiplying the amplitude by a correction factor $c_0 \; \Delta t/(2(\Delta x)^{d-1})$, where d is the number of dimensions. In addition, considering the match found between the system of coupled first-order wave equations and Green's function for homogeneous media, the Greens relation (7) implies that using the k-Wave solver for simulating propagation of ultrasound sources in d dimensions, modelling the emitters requires an integration of points sources over d dimensions. The readers are referred to [43] for more details. The users should check if these problems are addressed in the k-Wave 2 (II). The users are also encouraged to acknowledge the original works [39, 40, 41], and the corrections to inclusion of time-varying source [43], if the latter is included in the next versions of the k-Wave.

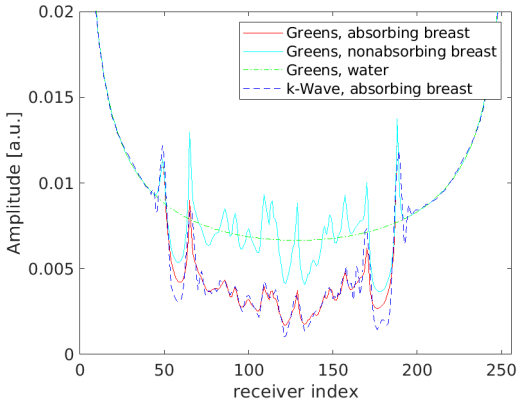

FIGURE 7. The amplitude of the pressure time series on all the receivers at single frequency 1 MHz after being produced by emitter 1. Using the Green's approach, the geometrical portion of the amplitudes is approximated via computing the rays' Jacobian using the paraxial ray equations (67).

APPENDIX-B. HOMOGENEOUS GREEN'S FUNCTION

Here, the Green's function for homogeneous media are defined. For a 2D homogeneous medium, the Green's function is in the form [3]

$$g_{0,2D}(\omega, \boldsymbol{x}; \boldsymbol{x'}) \approx \frac{1}{(8\pi\phi_0(\boldsymbol{x}; \boldsymbol{x'}))^{1/2}} e^{i(\phi_0(\boldsymbol{x};\boldsymbol{x'})+\pi/4)}. \tag{64}$$

For a 3D homogeneous medium, the Green's function is in the form [3]

$$g_{0,3D}(\omega, \boldsymbol{x}; \boldsymbol{x'}) = \frac{1}{4\pi|\boldsymbol{x} - \boldsymbol{x'}|} e^{i\phi_0(\boldsymbol{x};\boldsymbol{x'})}. \tag{65}$$

APPENDIX-C. AN ALTERNATIVE HAMILTONIAN

The Hamiltonian defined in (45) gives directly unit ray directions, i.e., $|d\boldsymbol{x}/ds| = 1$. The Hamiltonian can be defined in different ways. For example, the Hamiltonian can be defined as

$$H(\boldsymbol{x}, \boldsymbol{k}) = \frac{1}{2}\left(\boldsymbol{k} \cdot \boldsymbol{k} - k^2\right), \tag{66}$$

which yields the ray equations the same as in (49), and paraxial ray equations

$$\frac{d}{ds}\delta\boldsymbol{x} = \frac{\delta\boldsymbol{k}}{k}, \qquad \frac{d}{ds}\delta\boldsymbol{k} = \left(\frac{1}{k^2}\nabla k \nabla k^T + \frac{1}{k}\nabla^2 k\right)\delta\boldsymbol{x}. \tag{67}$$

The paraxial ray equations (67) are computationally cheaper than (50). However, the Hamiltonian in (45) gives directly unit directions, but using the Hamiltonian in (66), a change of variable has been performed in space for ensuring the unitary of the ray direction vector $d\boldsymbol{x}/ds$. Figure 7 shows the amplitudes at the single frequency 1 MHz on the receivers after being produced by emitter 1. In this figure, for the Green's approach, the geometrical portion of the amplitudes was approximated using the paraxial ray equations (67). A comparison between figures 3(b) and 7 shows that the paraxial ray equations derived using the Hamiltonians in (45) and (66) provide very similar amplitudes for the smoothed wavenumber field shown in figures 1(c) and 1(d).

References

[1] Ashkan Javaherian, ray-based-quantitative-ultrasound-tomography, 2022, `https://github.com/Ash1362/ray-based-quantitative-ultrasound-tomography/`

[2] Ashkan Javaherian, Transmission ultrasound data simulated using the k-Wave toolbox as a benchmark for biomedical quantitative ultrasound tomography using a ray approximation to Green's function, 2023, `https://doi.org/10.5281/zenodo.7717290`

[3] A. Javaherian and B. Cox, Ray-based inversion accounting for scattering for biomedical ultrasound tomography, *Inverse Problems* vol. 37, no.11, 115003, 2021.

[4] N. Duric P. Littrup, L. Poulo, A. Babkin, R. Pevzner, E. Holsapple, O. Rama and C. Glide, Detection of breast cancer with ultrasound tomography: First results with the Computed Ultrasound Risk Evaluation (CURE) prototype, *Med. Phys.* vol. 34, no.2, 2007.

[5] J. F. Synnevag, A. Austeng and S. Holm, Adaptive beamforming applied to medical ultrasound imaging, *IEEE transactions on ultrasonics, ferroelectrics, and frequency control*, Vol. 54, no. 8, pp. 1606-1613, 2007. DOI: 10.1109/TUFFC.2007.431.

[6] T. Hopp, N. Ruiter, J. C. Bamber, N. Duric and K.W.A. van Dongen (Eds.) 2017 International Workshop on Medical Ultrasound Tomography, Speyer, Germany.

[7] C. Li, N. Duric, P. Littrup and L. Huang, In-vivo breast sound speed imaging with ultrasound computed tomography, *Ultrasound in Med. & Biol.*, vol. 35, no. 10, pp. 1615–1628, 2009.

[8] N. V. Ruiter, M. Zapf, T. Hopp, R. Dapp, E. Kretzek, M. Birk, B. Kohout, H Gemmeke, 3D ultrasound computer tomography of the breast: A new era?, European Journal of Radiology, vol. 81, Supplement 1, pp. S133-S134, 2012.

[9] H. Gemmeke, T. Hopp, M. Zapf, C. Kaiser, N.V. Ruiter, 3D Ultrasound Computer Tomography: Hardware Setup, Reconstruction Methods and First Clinical Results, NUCL INSTRUM METH A, vol. 873, 2017, pp. 59-65, 2017.

[10] K. J. Opielinski, P. Pruchnicki, P. Szymanowski, W. K. Szepieniec, H. Szweda, E. Swis, M. Jozwik, M. Tenderenda and M. Bułkowskif, Multimodal ultrasound computer-assisted tomography: An approach to the recognition of breast lesions, *COMPUT MED IMAG GRAP* vol. 65,pp. 102–114, 2018.

[11] C. Li, L. Huang, N. Duric, H. Zhang, and C. Rowe, An improved automatic time-of-flight picker for medical ultrasound tomography, Ultrasonics., vol. 49, pp. 61-72, 2009.

[12] K. Wang, T. Matthews, F. Anis, C. Li, N. Duric, and M. A. Anastasio, Waveform inversion with source encoding for breast sound speed reconstruction in ultrasound Computed Tomography, *IEEE T ULTRASON FERR*, vol. 62, no. 3, 2015.

[13] G. Y. Sandhu, C. Li, O. Roy, S. Schmidt, and N. Duric, Frequency domain ultrasound waveform tomography: breast imaging using a ring transducer, *Phys. Med. Biol.*, Vol. 60, 5381–5398, 2015.

[14] J. W. Wiskin, D. T. Borup, E. Iuanow, J. Klock, M. W. Lenox, 3-D Nonlinear Acoustic Inverse Scattering: Algorithm and Quantitative Results, *IEEE T ULTRASON FERR*, vol. 64, no. 3, 2017.

[15] A. V. Goncharsky and S. Y. Romanov, Iterative methods for solving coefficient inverse problems of wave tomography in models with attenuation, *Inverse Problems*, vol. 33, pp. 025003, 2017.

[16] T. P. Matthews, K. Wang, C. Li, N. Duric, and M. A. Anastasio, Regularized Dual Averaging Image Reconstruction for Full-Wave Ultrasound Computed Tomography, *IEEE T ULTRASON FERR*, vol. 64, no. 5, 2017.

[17] S. Bernard , V. Monteiller , D. Komatitsch and P. Lasaygues, Ultrasonic computed tomography based on full-waveform inversion for bone quantitative imaging, *Phys. Med. Biol.* Vol. 62, pp. 7011–7035, 2017.

[18] F. Faucher and O. Scherzer, Adjoint-state method for Hybridizable Discontinuous Galerkin discretization, application to the inverse acoustic wave problem, *Computer Methods in Applied Mechanics and Engineering*, Vol. 372, 2020.

[19] L. Guasch, O. Calderón Agudo, M. Tang, P. Nachev, and M. Warner, Full-waveform inversion imaging of the human brain. *Nature Digital Medicine*, vol. 3, 28, 2020.

[20] Berkan Lafci and Elena Merčep and Joaquin L. Herraiz and Xosé Luís Deán-Ben and Daniel Razansky, Noninvasive multiparametric characterization of mammary tumors with transmission-reflection optoacoustic ultrasound, Neoplasia, Vol. 22, No. 12, 2020.

[21] F. Li, U. Villa, S. Park and M. A. Anastasio, 3-D Stochastic Numerical Breast Phantoms for Enabling Virtual Imaging Trials of Ultrasound Computed Tomography, *IEEE T ULTRASON FERR*, vol. 69, no. 1, pp. 135-146, Jan. 2022, doi: 10.1109/TUFFC.2021.3112544.

[22] A. J. Devaney, A filtered backpropagation algorithm for diffraction tomography, *Ultrason. Imag.*, vol. 4, pp. 336–350, 1982.

[23] A. J. Devaney and M. L. Oristaglio, Inversion procedure for inverse scattering within the distorted-wave Born approximation, *Physical Review Letters*, vol. (51), no. 4, 1983.
[24] W. B. Beydoun and A. Tarantola, First Born and Rytov approximations: Modelling and inversion conditions in a canonical example, *J. Acoust. Soc. Am.*, vol. 83, pp. 1045-1055, 1988.
[25] D. T. Borup, S. A. Johnson, W. W. Kimz and M. J. Berggren, Nonperturbative Diffraction tomography via Gauss-Newton iteration applied to the scattering integral equation, *Ultrasonic Imaging*, vol. 14, pp. 69-85, 1992.
[26] T.D. Mast, Aberration correction for time-domain ultrasound diffraction tomography, *J. Acoust. Soc. Am.*, vol. 112, no. 1, 2002.
[27] F. Simonetti, L. Huang, N. Duric, and P. Littrup, Diffraction and coherence in breast ultrasound tomography: A study with a toroidal array, *Med. Phys.*, vol. 36, pp. 2955, 2009.
[28] P. Müller, M. Schürmann, and J. Guck, ODTbrain: a Python library for full-view, dense diffraction tomography, BMC Bioinformatics, vol. 16, iss. 1, p. 1–9, 2015.
[29] N. K. Martiartu, C. Boehm, A. Fichtner, 3-D Wave-Equation-Based Finite-Frequency Tomography for Ultrasound Computed Tomography, *IEEE Transactions on Ultrasonics, Ferroelectrics, and Frequency Control*, Vol. 67, no. 7, pp. 1332 - 1343, 2020.
[30] Y. Fan and L. Ying, Solving inverse wave scattering with deep learning, *Annals of Mathematical Sciences and Applications*, Vol. 7, No. 1, pp. 23–48, 2022.
[31] F. Faucher, C. Kirisits, M. Quellmalz, and O. Scherzer, and E. Setterqvist, Diffraction Tomography, Fourier Reconstruction, and Full Waveform Inversion, In Handbook of Mathematical Models and Algorithms in Computer Vision and Imaging, 2022, doi. 10.1007/978-3-030-03009-4.
[32] P. Thierry, S. Operto, and G. Lambare, Fast 2-D ray+Born migration/inversion in complex media, *GEOPHYSICS*, Vol. 64, No. 1, pp. 162–181, 1999.
[33] V. Červený, Seismic ray theory, Cambridge University Press. 2001.
[34] P. Huthwaite and F. Simonetti, High-resolution imaging without iteration: a fast and robust method for breast ultrasound tomography, *J. Acoust. Soc. Am.*, vol. 130, no. 3, pp. 1721-34, 2011.
[35] S. Jin, R. Madariaga, J. Virieux, and G. Lambaré, Two-dimensional asymptotic iterative elastic inversion, *Geophys. J. Internat.*, Vol. 108, No.2, pp. 575–588, 1992.
[36] G. Lambare, J. Virieux, R. Madariaga, and S. Jin, Iterative asymptotic inversion in the acoustic approximation, *GEOPHYSICS*, Vol. 57. No. 9, pp. 1138-1154, 1992.
[37] G. Lambare, S. Operto, P. Podvin, and P. Thierry, 3D ray+Born migration/inversion—Part 1: Theory, *GEOPHYSICS*, Vol. 68, No. 4, 2003.
[38] A. Javaherian, F. Lucka and B. Cox, Refraction-corrected ray-based inversion for three-dimensional ultrasound tomography of the breast, *Inverse Problems*, vol. 36, 125010, 2020.
[39] N. N. Bojarski, The k-space formulation of the scattering problem in the time domain, *J. Acous. Soc.Am.*, vol. 72, 1982, pp. 570–584.
[40] T. D. Mast, L. P. Souriau, D. D. Liu, M. Tabei, A. I. Nachman, and R. C. Waag, A k-spacemethod for large-scale models of wave propagation in tissue, *IEEE Trans. Ultrason. Ferroelectr. Freq. Control*, vol. 48, 2001, pp. 341–354.
[41] M. Tabei, T. D. Mast, and R. C. Waag, "A k-space method for coupled first-order acoustic propagation equations," *J. Acoust. Soc. Am.* vol. 111, pp. 53–63, 2002.
[42] B. E. Treeby and B. T. Cox, k-Wave: MATLAB toolbox for the simulation and reconstruction of photoacoustic wave fields *J. Biomed. Opt.* vol. 15, no. 2, 021314, 2010.
[43] A. Javaherian, A note on an open-source toolbox for simulation of acoustic waves: inclusion of time-varying source, Arxiv, https://arxiv.org/pdf/2212.04466.pdf.
[44] J. F. Kelly, R. J. McGough, and M. M. Meerschaert, Analytical time-domain Green's functions for power-law media, *J. Acoust. Soc. Am.*, vol. 124, no. 5, pp. 2861–2872, 2008.
[45] T. L. Szabo, Time domain wave equations for lossy media obeying a frequency power law, *J. Acoust. Soc. Am.*, vol. 96, pp. 491–500, 1994.
[46] M. Liebler, S. Ginter, T. Dreyer, and R. E. Riedlinger, "Full wave modeling of therapeutic ultrasound: Efficient time-domain implementation of the frequency power-law attenuation, *J. Acoust. Soc. Am.*, vol. 116, pp. 2742–2750, 2004.
[47] Pierce A D 1981 Acoustics: An Introduction to its Physical Principles and Applications 3rd Edition (Berlin: Springer and ASA Press) (https://doi.org/10.1007/978-3-030-11214-1)
[48] J.C. Butcher, The numerical analysis of ordinary differential equations. Runge–Kutta and general linear methods, Wiley, 1987.
[49] E. Kreyszig, 1993 Advanced engineering mathematics. John Wiley &Sons, Inc., New York.

[50] J. Virieux and V. Ferra Ray tracing in 3D complex isotropic media: An analysis of the problem, *GEOPHYSICS*, vol. 56, no. 12, pp. 2057-2069, 1991.
[51] A. H. Anderson and A. C. Kak, Digital ray tracing in two-dimensional refractive fields, *J. Acoust. Soc. Am.*, vol. 72, pp. 1593-1606, 1982.
[52] V. ćervený, T. J. Moser, Ray propagator matrices in three-dimensional anisotropic inhomogeneous layered media, *Geophys. J. Int.* Vol. 168, pp. 593–604, 2007.
[53] Y. Lou, W. Zhou, T. P. Matthews, C. M. Appleton and M. A. Anastasio, Generation of anatomically realistic numerical phantoms for photoacoustic and ultrasonic breast imaging, *J Biomed Opt.*, vol. 22, no. 4, pp. 041015, 2017.
[54] B. Petrovic and S. Parolai, Joint Convulsion of Building and Downhole strong-motion recordings: evidence for the seismic wavefield being radiated back into the shallow geological layers, *Bulletin of the Seismological Society of America*, Vol. 106, No. 4, pp. 1720–1732, 2016, doi: 10.1785/0120150326.
[55] A. H. Anderson and A.C. Kak, Simultaneous algebraic reconstruction techniques (SART): A superior implementation of the ART algorithm, *Ultrasonic Imaging*, vol. 6, no. 1, pp. 81-94, 1984.
[56] k-Wave user manual, A Matlab toolbox for the time domain simulation of acoustic wave fields, Version 1.1, 27th August 2016 (the last version).
[57] F. Lucka, M. Perez-Liva, B. E. Treeby and B. T. Cox, High resolution 3D ultrasonic breast imaging by timedomain full waveform inversion, Inverse Problems, Vol. 38, 025008, 2022.
[58] A. Javaherian, "Variational approaches for photo-acoustic tomography," School of Mathematics, The University of Manchester, Manchester, UK, (2019).